Effects of CNTs in polymer nanocomposite pillars fabricated through Two-Photon Polymerization

Amanda Daokoon Inthavong

A thesis

submitted in partial fulfillment of the

Requirements for the Degree of

Master of Science

University of Washington 2021

2021

Committee:

Prof. Eleftheria Roumeli

Prof. Lucas Meza

Program Authorized to Offer Degree:

Material Science and Engineering

University of Washington

Abstract

Effects of CNTs in polymer nanocomposite pillars fabricated through Two-Photon Polymerization

Amanda Daokoon Inthavong

Chair of the Supervisory Committee:

Prof. Eleftheria Roumeli

Department of Material Science and Engineering

In recent decades, advancements in the synthesis and manufacturing of carbon nanomaterials such as carbon nanotubes (CNTs) have made such materials excellent candidates for reinforcing polymers, providing substantial contributions to the field of polymer nanocomposites. CNTs have been widely used in areas such as electronic devices, automotive, and the aerospace sectors to name a few. They offer excellent electrical, mechanical, and thermal properties making it a strong candidate as a nanofiller for polymer composites. Combining this material with the emergence of direct laser writing using 2-photon polymerization (2PP), we can now begin studying and understanding nanostructured nanocomposites. 2PP enables us the design freedom to create niche structures and provide theoretically unlimited component complexity. Therefore, opening the area of nano-architected materials.

In this work, printability and mechanical behavior of micro- and nano-pillars made from custom di(trimethylolpropane) tetra-acrylate polymer and 0.004wt% functionalized-CNT will be investigated. Pillars tested had an aspect ratio of 3 where diameters were targeted at 10um, 1um, 600nm, 500nm, 400nm and 300nm. For printability, parameter sweeps were conducted to determine optimal print parameters. Parallel to this, a post-processing study observed the influence of UV exposure and drying options on pillar geometry. As for mechanical testing, micro-compression testing was conducted on all pillars. In particular, size effects in pure polymer pillar structures fabricated via 2PP and effects of CNTs on the mechanical properties of polymer nanocomposites from micro-compression testing are targeted. Our findings demonstrate that CNTs enhanced mechanical properties of pillars with a diameter of 10um compared to their pure polymer counterparts. Though when investigating pillars with diameters 1um and below, the fabricated structures appear instable to satisfy the conditions required for compression testing, thereby prohibiting systematic conclusions for the case of the composites. On the contrary, for the pure polymer a strengthening and stiffening was observed for decreasing pillar diameters, confirming size-effects previously reported for amorphous thermoplastics.

This is to certify that I have examined this copy of a

master's thesis by: Amanda Daokoon Inthavong

And have found it complete and satisfactory in all respects,

and that any and all revisions required by the

final examining committee have been made.

Committee Members:

_____

Prof. Eleftheria Roumeli, Chair

_____

Prof. Lucas Meza

Date: 12/14/2021

Table of Contents

II. List of Figures

III. List of Tables

IV. Acknowledgments

First, I would like to sincerely thank my academic advisor, Prof. Eleftheria Roumeli, for being an incredible support and guide for the entirety of my master program. I am also grateful Dr. Andrew Jimenez, Dr. Paul Grandgeorge, Mallory Parker, and Jeffrey Lin for their invaluable support in this project. It would not have been possible to complete my research without them.

Lastly, I would like to thank Jeremy Fredricks, Konstantina Mason, Noah Werner, and all members from Prof. Roumeli's research group for being collaborative colleagues. Special thanks to Esther Law who has given me a great friendship for five years.

1. Introduction

Interest in composite material arises from their capabilities in combining superior properties of two or more constituent materials into one substance [6]. When one of these constituents has nanoscale morphology in the range of 10-100 nm, it is considered a nanocomposite [6]. Over the recent decades, polymer nanocomposites have gained interest in commercial sector applications. Not only do their properties depend on the original constituents, but also on their morphological and interfacial characteristics [6], [7]. These tunable characteristics can lead to enhanced performance in mechanical properties, thermal stability, electrical conductivity, and chemical resistance [6].

In terms of manufacturing, a prime area for polymer nanocomposites to be utilized is in additive manufacturing (AM). AM presents the opportunity of design flexibility and customizability for specific applications in three dimensions [8]. Though, the variety of materials and applications for AM is still limited [9]. Hence, it is important pursuing development of high performing materials to expand the capabilities of AM. This thesis will explore the effects of carbon nanotubes (CNTs) on printability and mechanical properties of polymer nanocomposites.

Recently, the increasing use of CNTs within polymetric matrices has enabled remarkable mechanical properties for polymer nanocomposites. Intrinsically, CNT properties possess outstanding mechanical performance where modulus, strength, and resilience are equal or above any current materials [10]. They also possess low mass density, high flexibility, and large aspect ratios typically ranging between 300 and1000 [11]. Also, due to the important stability rooted in their carbon-carbon bonds, pure CNTs are known to be one of the lightest and most robust nanomaterials [12]. From their unique structures, CNTs demonstrate exceptional thermal stability and electrical properties allowing for potential in a multitude of applications spanning from

quantum wires to molecular diodes [13]. Though, translation of CNT nanocomposites to AM technologies remains a challenge primarily due to difficulties in dispersing, aligning, and maintaining sufficient interfacial CNT-matrix bonds [14], [15].

1.1. Polymer Nanocomposites – Effects of CNTs

When fabricating polymer nanocomposites, filler choice is crucial in modifying properties. The desired properties can be elicited and tuned by changing the shape, volume fraction, and size of filler particles [6]. For this thesis, CNTs are the filler of choice as they are known to improve the mechanical properties of polymers at low concentrations [6]. An example of enhancement they can bring to nanocomposites is from Qian et al., where the authors used ultrasonication to mix 1 wt.% CNTs with polystyrene in toluene. In their study, they achieved a 25% increase in tensile strength and 36%-42% increase in elastic modulus compared to pure polystyrene [14]. Another example is by Dul et al., where they direct melt compounded ABS with CNTs. Results showed that at 6 wt%, the tensile strength and elastic modulus to break the nanocomposite sample were increased by 33% and 20%, respectively [16].

The CNTs used for this thesis are functionalized multi-walled carbon nanotubes (MWCNTs). Compared to unfunctionalized CNTs, the use of functionalized CNTs allows for better dispersion and mixing of the polymer nanocomposite, and is often used to promote covalent or physical interactions between the polymer and the filler [9]. The enhanced dispersion and interactions enable homogeneous mixtures despite the poor native interfacial interactions between CNTs and the polymer matrix. Also, commercialized CNTs often are heavily entangled bundles which contribute to difficulties in dispersion. Therefore, by developing methods to modify surface

properties, functionalization offers better interactions between the CNT filler and polymer matrix [17].

1.2. Two-Photon Polymerization

Stereolithography is a laser-based 3D printing technique which forms structures layer-by-layer via photochemical processes. At the molecular level, this technique utilizes light to cause monomers to polymerize [18]. Depending on the laser used, it is possible to print at the nanometer scale, therefore making two-photon polymerization capable of achieving the highest resolution out of all current printing [19]. Its capabilities in fabricating niche structures has allowed this technique to be a powerful tool in opening the area of nano-architected materials [20]–[22].

Two-photon polymerization (2PP) is a type of stereolithographic technique where the mechanism of reaction involves the simultaneous absorption of two photons resulting in a direct excitation of molecules without the presence of an intermediate state [23]. It is particularly known for its capabilities in fabricated well-defined micro and nano-structures for its resolution beyond the diffraction limit [24]. A femtosecond pulsed laser is used to allow the necessary condition for two photons to be absorbed simultaneously resulting in a high light intensity [25]. This mechanism was first described by Maria Göppert-Mayer in 1931 but the technology was unavailable in laboratories until the 1980's [26]. Figure 1 reports how the print is achieved through 2-photon absorption (2PA) compared to 1-photon absorption (1PA). The most distinguishable difference is the distribution of energy intensity from each. 1PA results in a wider distribution of necessary energy to trigger polymerization as seen in the blue and green shaded 1PA regions of Figure 1b and 1c, respectively [1]. The consequence is a polymerized hourglass-like shape across a significant thickness of the resin. On the other hand, 2PA has a more localized energy intensity

distribution resulting in a sphere-like shape of polymerized resin called a voxel. A voxel is a unit volume which is the building block to create discrete 3D structures similarly to how pixels can form an image. This allowed for build with larger complexity than compared to 2PA polymerization [1].

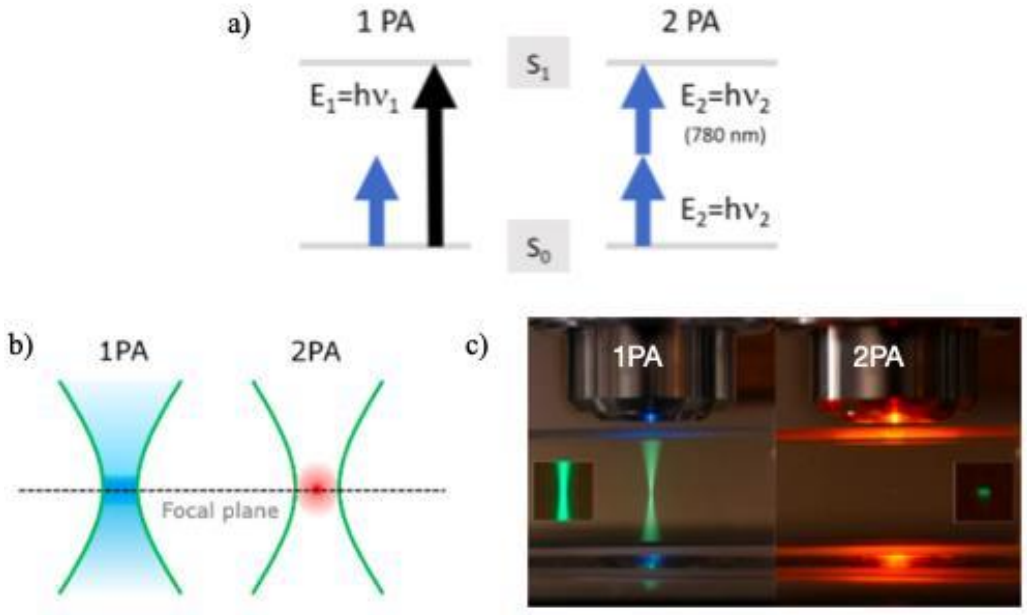

Figure 1. a) Schematic of one-photon and two-photon absorption, where S1 represents the necessary energy level for polymerization to occur. b) A representation of intensity distribution for one-photon and two-photon absorption. c) Image of fluorescence from one-photon and two-photon absorption processes. Reproduced from [1].

The chemical reactions involved in 2PP can be divided into five sequential steps: 1) Dissociation; 2) Initiation; 3) Propagation; 4) Termination; 5) Oxygen Quenching [27]. The following equations outline the mentioned steps [27]:

$$\mathrm{I} \xrightarrow{2h\nu} \mathrm{I}^* \rightarrow 2\mathrm{R}\cdot \qquad \text{Dissociation}$$

$$\mathrm{R}\cdot + \mathrm{M} \rightarrow \mathrm{M}_1\cdot \qquad \text{Initiation}$$

$$\mathrm{M}_n\cdot + \mathrm{M} \rightarrow \mathrm{M}_{n+1}\cdot \qquad \text{Propagation}$$

$$\mathrm{M}_n\cdot + \mathrm{M}_m\cdot \rightarrow \mathrm{X} \qquad \text{Termination}$$

$$\mathrm{M}_n\cdot + \mathrm{O}_2 \rightarrow \mathrm{M}_n - \mathrm{OO}\cdot \qquad \text{Oxygen Quenching}$$

In the first step, dissociation of the initiator, I, creates two radical species, R·, as two photons with energy *hv* undergo absorption [27]. This step is then followed by the addition of a single monomer, M, to the initiation radical resulting in the formation of reactive monomers, M_1·. Next, propagation occurs where additional monomers are added to the reactive monomer species [28]. To stop this chain reaction, termination occurs. This is where inert molecules are formed from the reactive species. Finally, oxygen quenching takes place. Here, oxygen has significant influence on the reaction kinetics in polymerization processes by reacting with radicals to form peroxyl radicals which increase termination, thereby leading to an inhibition of polymerization [27].

1.2.1. Nanocomposite materials fabricated through Two-Photon Polymerization

Over the last years, there has been growing interest in developing new photoresist materials compatible with the free form capabilities and tailored properties for 2PP [29]. Combining the flexibility of 3D printing design with nanocomposites' tunability can potentially serve as the driving force in future material design. In this section, we will highlight several papers focusing on nanocomposite materials fabricated via 2PP.

One area of focus is on improving the mechanical properties of polymeric materials. Doing so may allow for increased complexity of printable structures while also avoiding their collapse

during developmental and drying stages [3]. Several papers have discussed the enhancement of Young's modulus, *E*, by dispersing single-walled carbon nanotubes (SWCNTs) and MWCNTs. For example, the Lu group studied an acrylate-thiol-based photosensitive resin containing dispersed MWCNTs. They found that adding the MWCNTs increased *E* and hardness and reduced shrinkage from 4% to 2.4% [2], [30]. The first indicator of improved mechanical performance was visually observed through Scanning Electronic Microscopy (SEM) images of their microbridge samples as seen in Figure 2. The bridge made of pure acrylate resin deformed while the same structure with 0.1wt% MWCNTs incorporated remained straight with no obvious signs deformation. Using nanoindentation, they measured *E* values of 1.35 GPa and 1.90 GPa and hardness values of 43 KPa and 67.5 Kpa for the acrylate resin and composite resin, respectively [2].

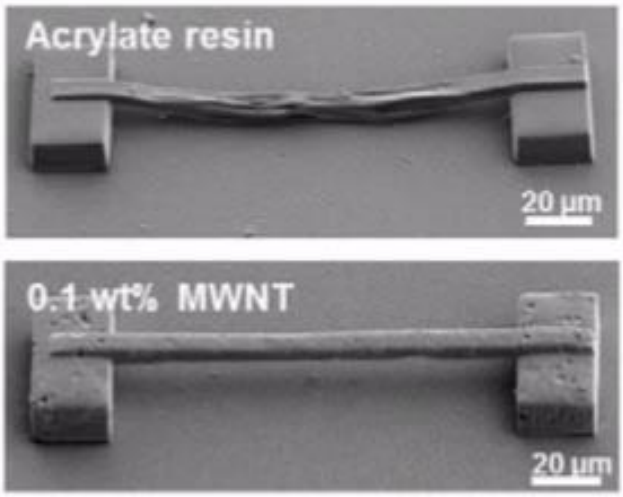

Figure 2. SEM images of microbridge structures composed of acrylate resin (top) and 0.1wt% MWCNT composite (bottom). Reproduced from [2].

Another area of interest is conductive nanocomposites. By adding conductive nanofillers, conductive properties can be elicited in otherwise insulative materials. For instance, this approach can be used for 3D conductive paths to enable connections within micro-electrical mechanical

systems (MEMS) [31]. Examples of conductive fillers are CNTs [2], crosslinking of metal nanoparticles [32], and functionalized magnetic nanoparticles [33].

Optical properties are also an area of how nanofillers can better polymeric material. The capability to print complex microstructures with high refractive index and tunable bandgaps can bring various applications in photonics, optics, and optical coatings [31]. While this thesis focuses on mechanical properties, we hope that the described fabrication and testing methods will be helpful in the other important research areas of nanocomposites fabricated via 2PP..

1.2.2. Degree of Polymerization and Post-Processing Effects

While printability of polymer nanocomposite structures from 2PP is key, another crucial area of thought is post-processing. Specifically, special care is required when handling micron-scaled samples as they are extremely susceptible to failure due to either human errors or environmental stimuli outside the print apparatus. For example, these delicate structures tend to have insufficient mechanical stability against capillary forces during developer evaporation [3]. The result can be the deformation or collapse of structures. This section will discuss literature optimizing post-processing procedures to ensure pristine sample conditions and optimize the degree of polymerization.

To enhance mechanical stability, Purtov et al. utilized Ultraviolet (UV) curing during post-processing of their polymer nanopillar structures [34]. Their nanopillars ranged from diameters of 120nm to 430nm and heights of 330nm to 1315nm. The authors observed shrinkage relating to the smaller pillars due to the reduction of laser power. The number of unreacted and non-covalently bound oligomers increased by reducing the laser power. Also, the distance between voxels was kept constant, making it so voxel overlap decreased, contributing to an incomplete cross-linking

reaction [34]. To combat this, Purtov et al. added a UV curing step while the structures were developed in isopropanol. The additional UV cure led to further cross-linking reactions, providing higher resistance against capillary forces and better mechanical stability [34]. In other words, it would allow for an increase in the degree of polymerization (DOP) in these structures. DOP is defined by the number of repeating units within a polymer chain and correlates to the molecular weight of the polymer [35]. Both physical and mechanical properties depend on the molecular weight and hence, on the DOP. For example, work by Bauer et al. characterized the mechanical properties of two-photon polymerized acrylate-based resin IP-Dip. Results demonstrated a proportional linear dependency of Young's Modulus and yield strength with the degree of conversion. In this case, the degree of conversion is the extent of cross-linking between polymer chains [36]. Therefore, increasing the DOP boosts entanglement of the chains from the increase of molecular weight, leading to enhancement of mechanical performance due to more efficient load transfer [35]. To better visualize the process, Figure 3 provides an overview of the post-processing procedure [3].

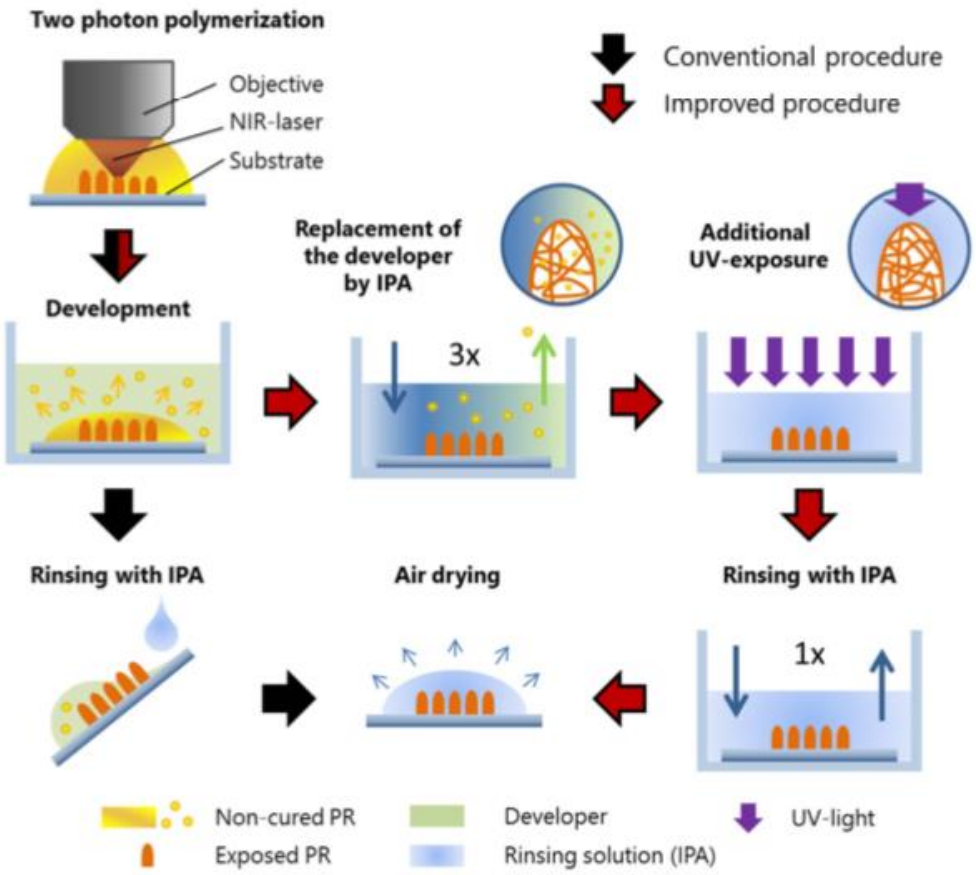

Figure 3. Schematic process flow of the conventional (black arrows) and improved UV-Cure wet development (red arrows) procedures of nanostructures. Reproduced from [3].

Along with UV curing, supercritical drying is another technique to ensure mechanical stability by reducing the surface tension [37]. Using this approach, nanostructures are developed in a supercritical fluid. This fluid behaves as both a diffusible liquid and a high-density gas. As a result, within this drying process, there is essentially no liquid/gas interface [37], hence causing a reduction in surface tension and forces on the nanostructures. In another study by Purtov et al., the authors acknowledged the benefits of critical point drying. Still, they excluded it from their work because it is a relatively time-consuming process [3]. This thesis will incorporate a combination of UV curing and critical point drying into the post-process. Such steps will be further discussed in Section 2.2.

1.3. Objectives

The foundation of this thesis was set down by Roumeli et al. in their work regarding polymer nanocomposite bend and stretch dominated micro-lattices [38]. They sought to understand size effects in nanostructured materials through micro-compression experiments. Results showed that presence of CNTs increased stiffness of cured photoresist by a factor of 2. Then, when the radius of the beams composing the truss structures was decreased from 1.8nm to 800nm, stiffness increased by a factor of 6 [38]. While a larger picture of improvement of CNT-based nanocomposites is shown, size effects may still be in question. The fundamental question of how structural design may influence the calculated mechanical properties requires more investigation, as it may potentially mask the true behavior of the material at the nanoscale. This thesis seeks to explore the true material behavior through the micro-compression of polymer and nanocomposite pillars. The objectives are to:

1) Observe size effects in pure polymer pillar structures fabricated via 2PP.
2) Observe effects of CNTs on mechanical properties of polymer nanocomposites.
3) Quantify the effect from CNTs and how they affect size effects.

Overall, this thesis will be structured as follows. To begin, Section 2 will review the materials and methods employed in this work. Next, Section 3 will provide results and discussion of 2PP printability and micromechanical testing of the pure polymer and nanocomposite pillars. Finally, Section 4 will lay out concluding remarks and outlook for future research.

2. Material and Methods

2.1. Materials

Two types of photoresists were fabricated, a pure polymer photoresist and a polymer CNT nanocomposite photoresist. A solution of di(trimethylolpropane) tetraacrylate used as monomer and a solution of 2-benzyl-2-(dimethylamino)-4′-morpholinobutyrophenone used as a photoinitiator were homogenized in a 10:1 mass ratio using a QSonica Probe Sonicator with a max power of 700 Watts. Amplitude was set to 10 and then ramped up manually to 100 within 30 seconds of starting the tool. A pulse mode was also enabled on the sonicator with 0.2 seconds off and 0.3 seconds on. The molecular structures of the monomer and photoinitiator are reported in Figure 4. As for the nanocomposites, MWCNTs and a thiol functionalizing agent were added to the pure polymer mixture. The result was a 0.004wt% functionalized-CNT (fCNT) polymer nanocomposite photoresist. The MWCNTs were commercially sourced and have lengths of 10-50um, inner diameter 3-5nm, outer diameter 8-15nm, and bulk density ~0.27 g/cm^3 (Cheaptubes, product 030102)[39]. Then, 5,5′-bis(mercaptomethyl)-2,2′-bipyridine in 20 wt.% on CNTs mass was used as the thiol functionalizing agent. The reason for functionalizing with a thiolizing agent is to promote interactions between the otherwise non-interacting polymer matrix and CNTs. Literature reports show strong covalent interactions between the acrylic polymers and thiol groups [40], [2], [41] while CNT thiolization is also reported, thereby justifying our choice for a thiolizing agent to promote adhesion and interactions between the acrylic backbone and the CNTs.

Prior results obtained by Roumeli et al. indicated that the 20 wt.% concentration and using Thiol as a functionalizing agent results in maximum modulus and compressive strength in lattices [38].

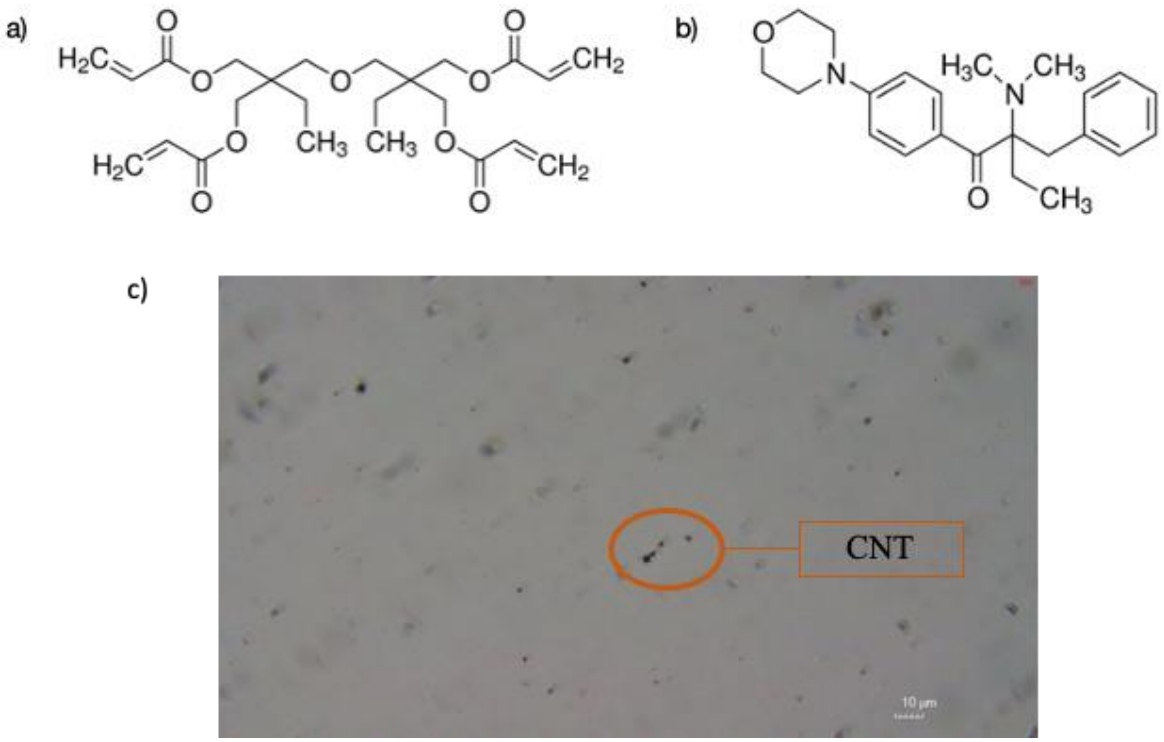

Figure 4. Molecular structures of (a) di(trimethylolpropane) tetraacrylate [4] and (b) 2-benzyl-2-(dimethylamino)-4′-morpholinobutyrophenone [5]. (c) Light Optical Microscopy image of 0.004wt% fCNT-polymer nanocomposite photoresist.

2.2. Two-Photon Polymerization System

2.2.1. Methodology for Optimizing Printability

Polymeric and nanocomposite micro-and nano- pillars with a target aspect ratio of 3 were printed with a Photonic Professional GT (Nanoscribe GmbH) at the Washington Nanofabrication Facility. This direct laser writing system uses a FemtoFiber pro-NIR laser with a center wavelength of 780nm, a repetition rate of 80 MHz, and a pulse width of ~100fs. The objective installed was a Plan-Apochromat 63 × 1.4 Oil DIC M27. As for sample preparation, the apparatus contained a 10x10mm silicon wafer, Kapton tape as spacers, a resin droplet, and a transparent coverslip. This set up is visually shown in Figure 5.

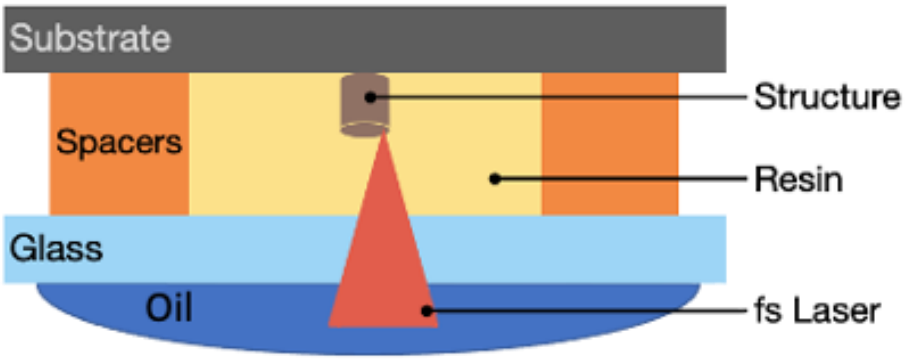

Figure 5. Schematic of 2PP sample apparatus.

To determine optimal print parameters for these nano- and micro-pillars, parameter sweeps were conducted. This involves fabricating pillars across a range of print parameters in a 5x5 matrix and visually examining their quality by either a Laser Scanning Microscope (LSM) or a Scanning Electron Microscope (SEM). In particular, the effects of laser power and scan speed were examined as reported in Table1. Table 2 provides an overview of the ranges used.

Table 1: Parameter sweep matrix for pure polymer 500nm diameter pillars.

Best	LP	80	85	90	95	100	
Slight Lean/Con	SS	400	400	400	400	400	
Hole, Heavy Lean/Cone				Slight Lean/Coni	Coning	Coning	y=4
Exploded, Melted or absent		80	85	90	95	100	
		350	350	350	350	350	
				Coning	Coning	Coning	y=3
		80	85	90	95	100	
		300	300	300	300	300	
				Coning	Coning	Coned	y=2
		80	85	90	95	100	
		250	250	250	250	250	
			Coning	Coning	Coning	Coning	y=1
		80	85	90	95	100	
		200	200	200	200	200	
		Coning	Coning	Coning	Coned	Coned	y=0
		x=0	x=1	x=2	x=3	x=4	

Table 2: Laser power and scan speed ranges for the parameter sweeps of pillars.

		Pure Polymer		Composite	
Pillar Diameter	**Writing Mode**	**Laser Power [%]**	**Scan Speed [µm/s]**	**Laser Power [%]**	**Scan Speed [µm/s]**
10um	**Galvo**	50-70	3000-6000	50-70	3000-6000
1um	**Piezo**	65-100	150-600	65-100	150-600
600nm	**Piezo**	65-100	150-600	80-100	150-450
500nm	**Piezo**	80-100	200-400	80-100	150-450
400nm	**Piezo**	65-100	150-600	80-100	150-450
300nm	**Piezo**	65-100	150-600	80-100	150-450

Due to their larger size, pillars with a diameter of 10um were printed in Galvo mode. As for pillars of diameters 1um and below, these were printed in Piezo mode, as noted in Table 1. What distinguished these two modes apart are their speeds and mechanisms. Galvo is more commonly recommended because of its speedy print capabilities being approximately 100x faster than Piezo [42]. As for the mechanism, Galvo uses a slightly different approach than Piezo. Galvo scans in the *XY* plane, and either the piezo or microscope z-drive controls z-axis shift [43]. With Piezo, it involves the movement of the substrate within the sample holder in all *x*-,*y*-, and *z*-directions [43]. Therefore, Piezo is recommended for complex high accuracy prints while Galvo for layer-by-layer larger structures.

2.2.2. Post-Processing Effects

To further optimize pillar quality, post-processing effects were examined. Based on previous work done by Roumeli et al., these nano-printed samples were processed in Propylene glycol methyl ether acetate (PGMEA) and isopropyl alcohol (IPA). The pillars and substrate apparatus were developed in a PGMEA, IPA, and Ultra-Pure IPA sequence. Then, the impact of UV exposure, critical point drying (CPD), and air drying processed were observed. WNF provided

the high-intensity UV lamp used for exposure. It was a BlueWave 200 lamp by Dymax USA, with a 300-450nm emission spectrum, as seen in Figure 6. Table 2 outlines the post-processes studied. To save time and work needed, the 1um pillar parameter sweeps for both composite and pure polymer underwent this post-processing study.

Table 3: List of Post-Processes and their steps.

Post-Process Number	Description of Post-Process	Steps within the Post-Process
1	Pillars CPDed, No Curing	1) 5min PGMEA 2) 5min IPA 3) 5min Ultra-Pure IPA 4) CPD
2	Pillars UV Illuminated during Pure IPA step + CPDed	1) 5min PGMEA 2) 5min IPA 3) Ultra-Pure IPA +UV Lamp 4) CPD
3	Pillars UV illuminated during Pure IPA step before air drying	1) 5min PGMEA 2) 5min IPA 3) Ultra-Pure IPA +UV Lamp 4) Air Dry
4	Pillars are air dried	1) 5min PGMEA 2) 5min IPA 3) 5min Ultra-Pure IPA 4) Air Dry
5	Pillars CPDed + UV post cure (300 sec)	1) 5min PGMEA 2) 5min IPA 3) 5min Ultra-Pure IPA 4) CPD 5) UV Lamp 5min
6	Pillars CPDed + UV post cure (60 sec)	1) 5min PGMEA 2) 5min IPA 3) 5min Ultra-Pure IPA 4) CPD 5) UV Lamp 5min

Figure 6. Set up of high-intensity UV BlueWave 200 lamp at WNF.

2.2.3. Calculating DOP via Raman Spectroscopy

To determine DOPs of cured pure polymer and nanocomposite pillars, Raman spectroscopy was done on a Renishaw InVia Raman Microscope at the Molecular Analysis Facility (MAF) at the University of Washington. The complete apparatus contains an InVia Spectrometer, a set of high-power lasers (785nm and 514nm), and a Leica DM IRB microscope. For the measurement parameters on cured samples, we used a 785nm excitation laser, 50x objective with a 0.5mm working distance, 50% laser power, and allowed for 10 seconds of accumulation time. As for the liquid resin, a 10x objective with a working distance of 11mm was used to avoid any objective damage. Once the raw spectra data was obtained, a 5^{th} order polynomial fitting was done for baseline subtraction in the Renishaw WIRE software. Figure 7 shows the instrument and fitting.

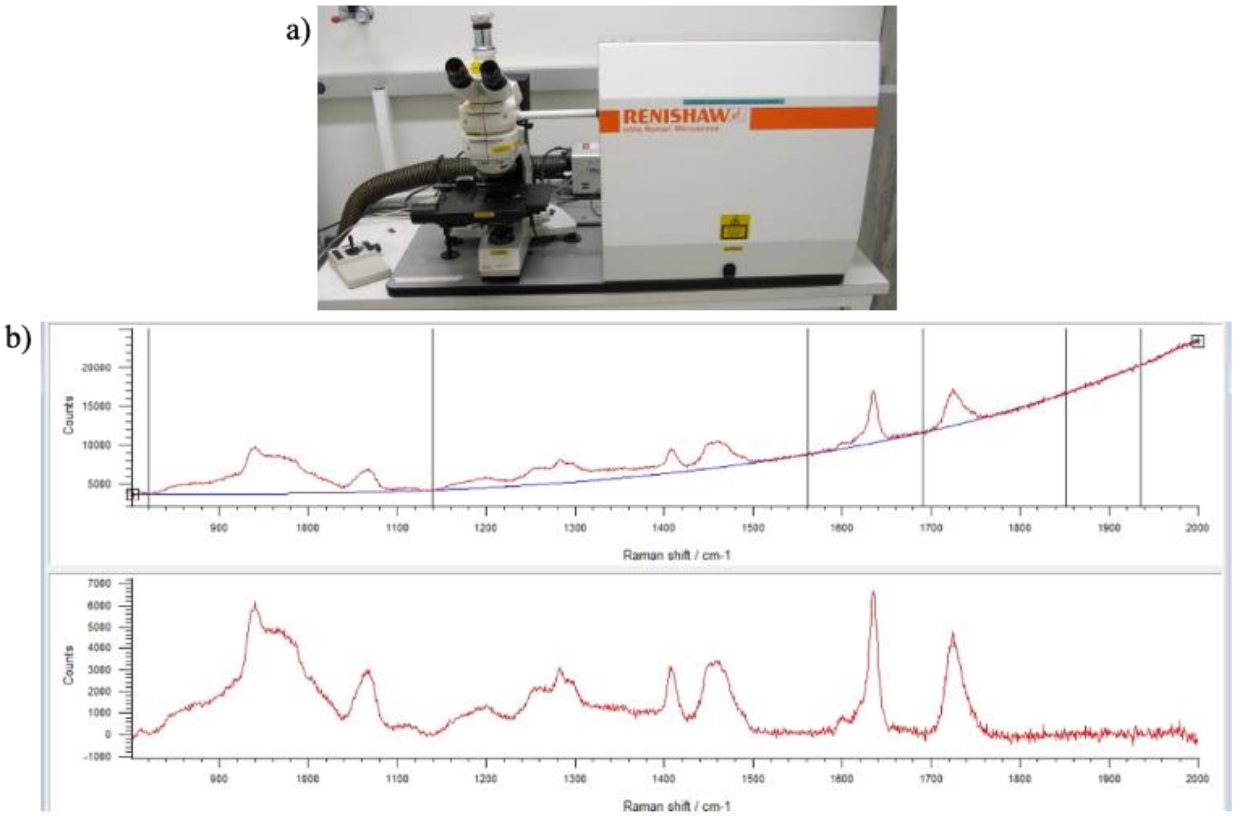

Figure 7. a) Image of InVia raman spectroscopy apparatus in the MAF. b) An example of spectra plots before (top) and after (bottom) the Renishaw WIRE software baseline subtraction applied.

Calculating the DOP involves the relative change of area under the C=C peak at 1635cm^{-1} with respect to the C=O peak at 1725cm^{-1} of the liquid resin before and after polymerization. To find the area under these peaks, the Voigt function was used in the Renishaw WIRE software. The following equation best highlights the relation for DOP with these areas [44], [45]:

$$DOP\% = 1 - \frac{\frac{A_{C=C}}{A_{C=O}}}{\frac{A^{\text{resin}}_{C=C}}{A^{\text{resin}}_{C=O}}} \times 100 \qquad (1)$$

2.3. Micromechanical Testing

2.3.1. Micromechanical Testing Apparatus

Micromechanical testing of the pillars was performed on an FT-MTA03 (FEMTO TOOLS, Switzerland) system. Two types of probes were used depending on the pillar size being tested. A flat punch tip with 100x50um^2 square contact area and max force of 20,000uN was used on the 10um diameter pillars. As for the smaller pillars of 1um diameter and below, a spherical tip with diameter of 50um and max force of 200uN was used. The reason for using two probes for our studies is to minimize signal to noise ratio (improve measurement resolution for the differently sized pillars). Upon testing the smaller pillars, force drifting was seen when the flat punch probe was idle above the pillar sample. Such drift is particularly concerning as its magnitude is a significant fraction of the max force seen in the pillars tested. This resulted in skewing the measurements. The solution was to use a higher resolution probe attainable through the spherical tip probe. Though with the spherical tip, concern arises regarding the influence of curvature geometry on the contact area of the pillars during compression. For the case of the 10um, this concern would apply as the pillar diameter is approximately 1/5 of the probe diameter, making it more likely for the curvature to impact measurements. As for the pillars 1um in diameter and below, the area at contact is assumed to be so small that curvature influence is neglected. The spherical tip measurements were performed with the pillar's central axis as close to the center of the tip as possible.

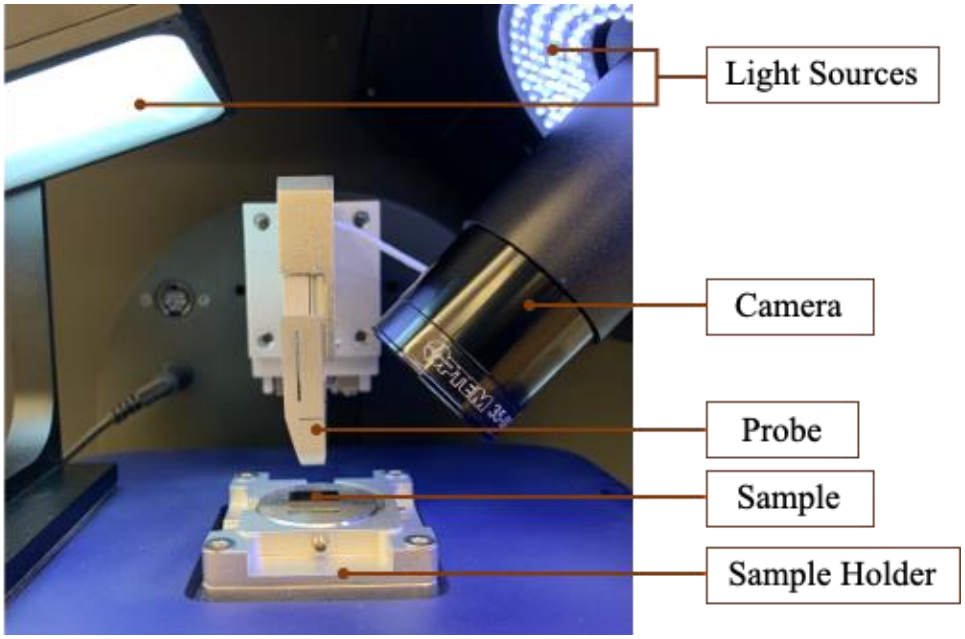

Figure 8. Micromechanical testing apparatus.

2.3.2. Micromechanical Testing Analysis

The force-displacement data were exported from the FT-MTA03 system for each pillar. Stiffness (k) was determined as the line of best fit slope in the elastic region with the magnitude of displacement varying from 0.1-0.2um depending on pillar size. The yield force (F_y) was identified as the force peak after the elastic region for pillars with diameters of 1um and below seen in Figure 9b. As for the 10um diameter pillars, the yield point was determined as the point on the force-displacement curve horizontal to the intersection of the linear elastic region and linear plastic region as seen in Figure 9a.

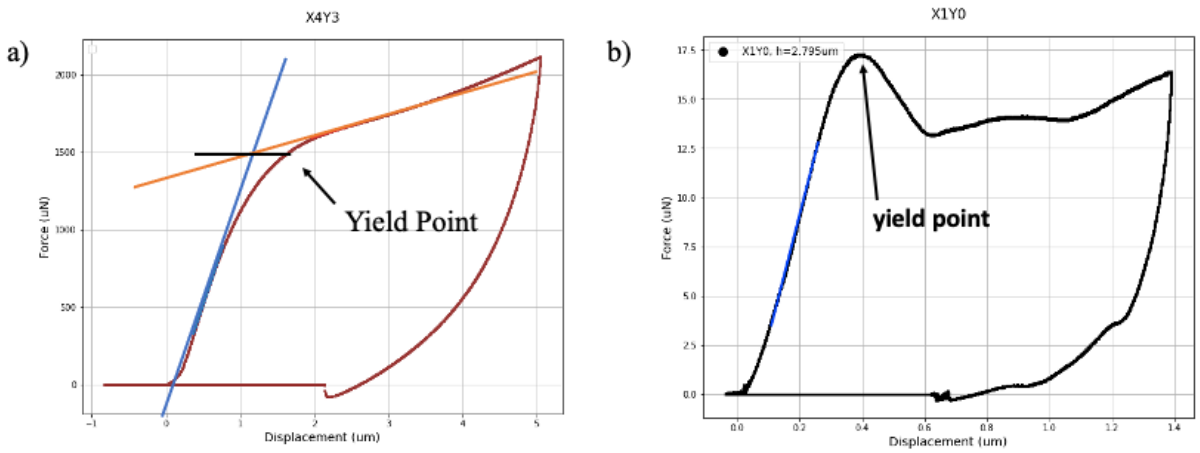

Figure 9. Identification of yield point on (a) a 10um diameter and (b) 500nm diameter pure polymer pillar force-displacement plot.

Elastic Modulus (E) and Strength (σ) were then determined using pillar geometry and the obtained stiffness and yield force values. Elastic Modulus was calculated using the following formula, where h and A respectively denote the measured pillar height and cross-sectional area:

$$E = \frac{kh}{A} \qquad (2)$$

Strength was then calculated using the following formula:

$$\sigma = \frac{F_y}{A} \qquad (3)$$

Defining the area and pillar height was straightforward for the 10um diameter pillars due to their conformity to a cylindrical shape seen in Figures 10a and 10b. The top view was used to measure the circular cross-sectional area. Pillar height was measured using the side view image at a 42-degree tilt.

As for smaller pillars of 1um and below, their structures were not ideally cylindrical. Instead, they were printed as conical-like structures where the top views showed an elliptical shape rather than circular, as seen in Figure 10d. Such niche geometries presented a challenge in assessing the geometrical properties of the pillars, particularly the cross-sectional areas. As noted, cross-sectional area and pillar height are crucial pillar features to define when determining Young's modulus and strength. To compute the mechanical properties of the pillars despite these geometrical imperfections, three approaches were used to calculated the cross-sectional area: (1) use the pillar base area, (2) use the tip area at the indentation height with no volume conservation, and (3) use the tip area accounting for volume conservation. Each of these approaches will first be outlined, and then the optimal method will be discussed further.

To start, the first method of determining cross-sectional area was to equate it to the base area of the pillar. Using the top view of the pillars seen in Figure 10e, the semi-major axis and semi minor axis of the elliptical were defined and the area (A_e) was calculated using the following equation:

$$A_e = \frac{\pi}{4} \times [Major\ Axis] \times [Minor\ Axis] \quad (4)$$

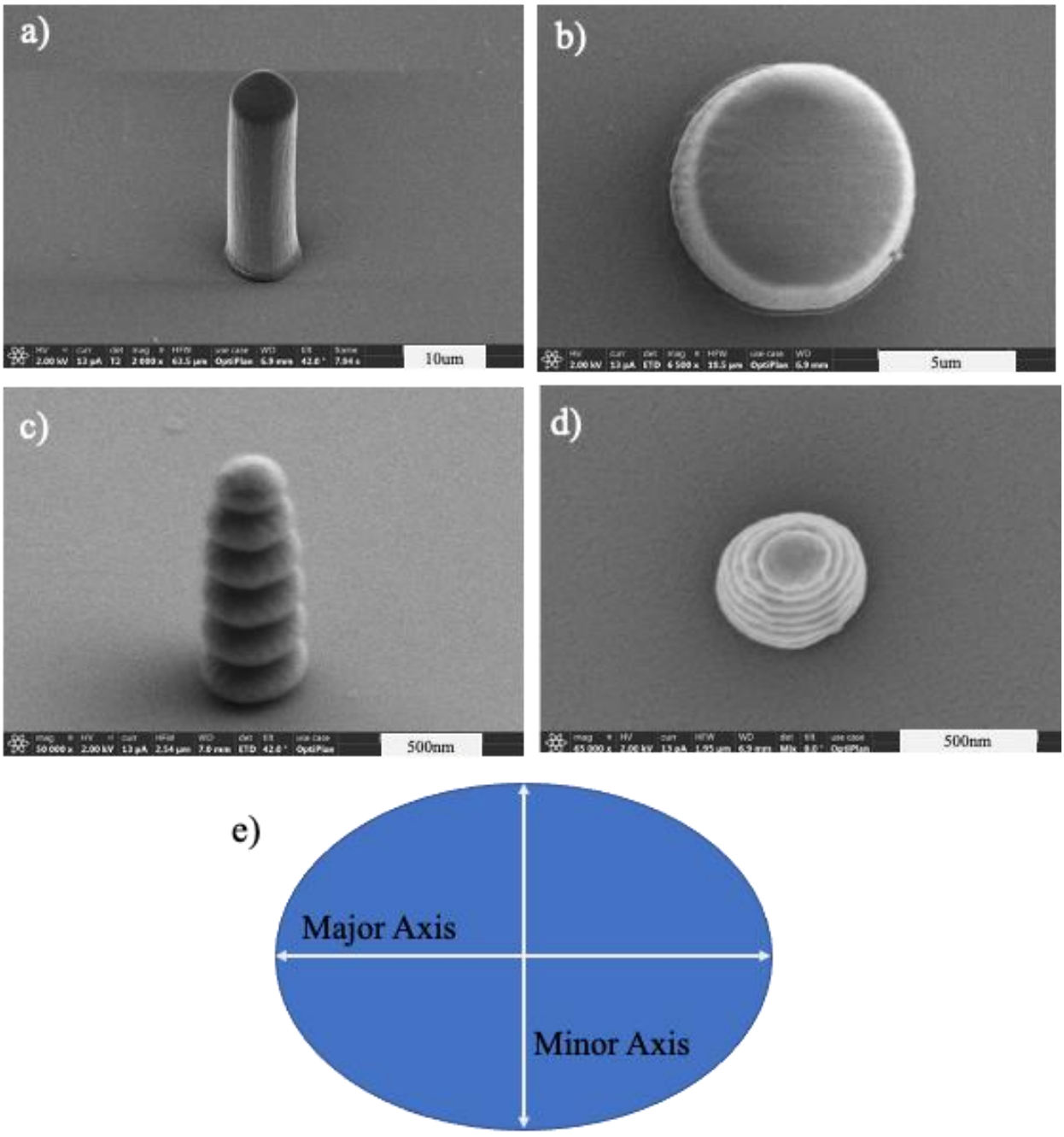

Figure 10. SEM images of targeted 10um diameter pillars for (a) 43 degree view and (b) top view. SEM images of targeted 300nm diameter pure polymerpillars for (a) 43 degree view and (b) top view. (e) Schematic of an ellipse with major and minor axis located.

To allow for comparison between the pillars, an apparent circular diameter ($D_{\mathrm{App,Base}}$) was back-calculated from the elliptical area as expressed in the following equation:

$$D_{\mathrm{App,Base}} = \sqrt{\frac{4A_e}{\pi}} \tag{5}$$

The second approach was to not account for volume conservation where tip area of the pillar was defined at the height of the probe. Here, the cross-sectional area was defined by the total displacement of the compression. By utilizing the rule of similar triangles, the cross-sectional area could be defined at the displacement of testing. Figure 11 provides a representative schematic showing how a pillar after compression would be interpreted with no volume conservation accounted. Below, the radius ($R_{\mathrm{App,NoVol}}$) used to calculate this cross-sectional area is provided where H is height, d is displacement, R_{base} is the radius of the base, and R_{top} is the radius of the top surface:

$$R_{\mathrm{App,NoVol}} = \frac{HR_{\mathrm{base}}^2 - (H-d)R_{\mathrm{base}}^2 + (H-d)R_{\mathrm{base}}R_{\mathrm{top}}}{HR_{\mathrm{base}}} \tag{6}$$

The final approach uses the assumption of volume conservation based on the Greer group's paper regarding micro-compression of pyramidal shaped structures [41]. Derivations were performed with similar methodology, but two aspects were changed to accommodate our pillar geometry. First, the cross-sectional area was defined as a circle. Second, cross-sectional areas were defined as the area after total displacement. Figure 11 provides a visualization. Ultimately, the radius used to determine cross-sectional area was determined by the following equation:

$$R_{\text{App,Vol}} = \frac{R_{\text{base}}}{2}\left[\sqrt{\frac{(9+4X)H+3d}{H-d}} - 1\right] \quad (7)$$

where X, γ, and β are defined as:

$$X = \gamma^2 - 3\gamma \quad (8)$$

$$\gamma = 1 - \beta \quad (9)$$

$$\beta = \frac{R_{\text{top}}}{R_{\text{App,Vol}}} \quad (10)$$

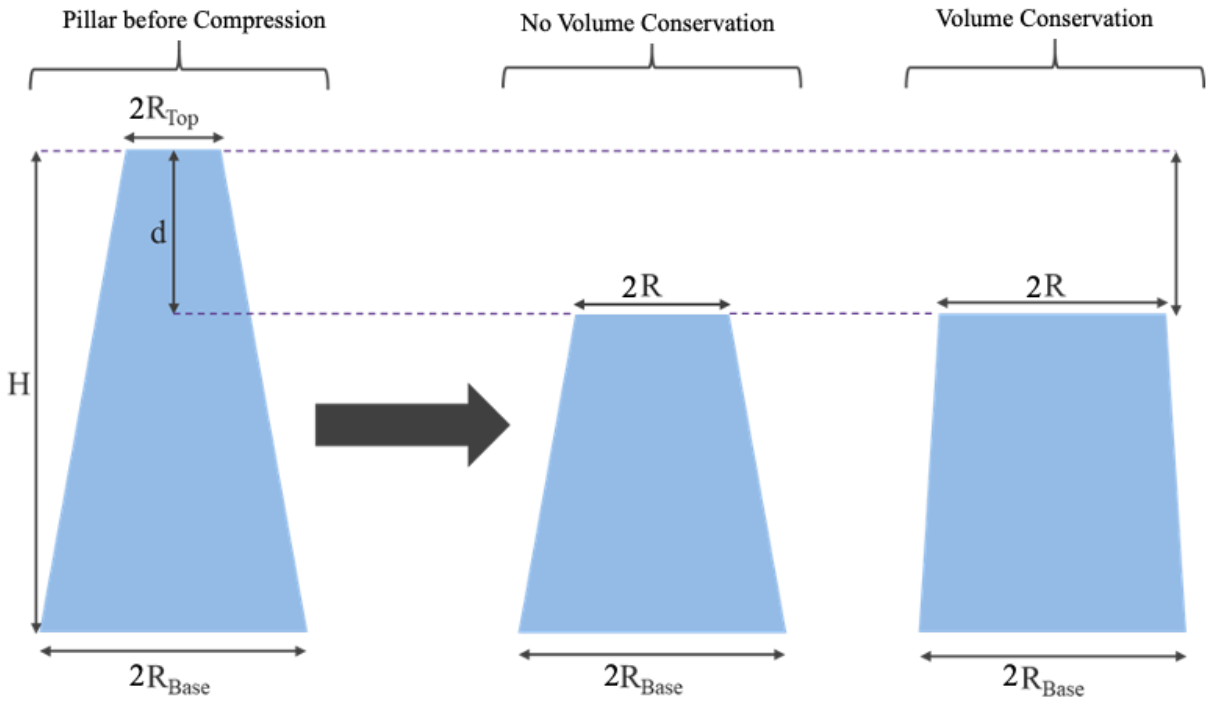

Figure 11. Labeled schematic of pillars before compression and post-compression.

2.4. Microscopy Methods

2.4.1 Laser Scanning Microscopy (LSM)

LSM was used to image and evaluate 10um pillar parameter sweeps. Here, an Olympus OLS 4100 optical profilometer from the Washington Clean Energy Testbeds (WCET) was used with a MPLAPONLEXT100 objective lens installed. While the instrument does not enable imaging of the pillar's side view, it does provide visualization of the top view, cross section, and height as seen in Figure 12. Therefore, evaluation of print quality was based on the circularity of the top view, pillar side profile, and how close the measured height and diameter were to their respective target values.

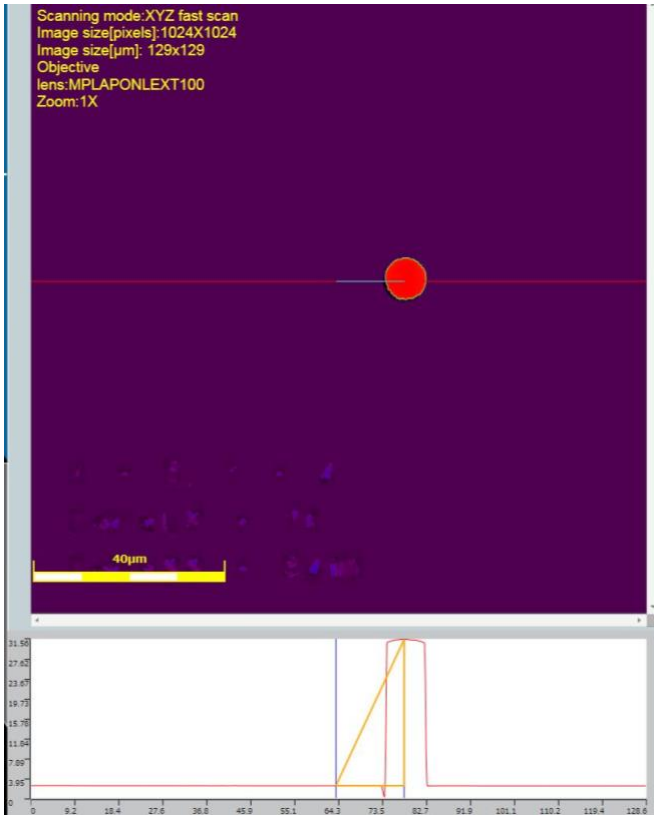

Figure 12. An example of the software screen for one 10um diameter pillar in the parameter sweep. Visualization of the top view is given along with a cross-sectional profile (bottom).

2.4.2 Scanning Electron Microscope (SEM)

To evaluate parameter sweeps of smaller diameter pillars 1um and below, an Electron Back-Scattered Diffraction (EBSD) – Apreo SEM was used with a voltage of 2kV and a current of 13pA as seen in Figure 13. Prior to inserting the samples into the tool, they were coated with 5nm platinum in a Leica EM ACE600 sputter coater. Images were acquired in a mixed BSE/SE (50%/50%) mode. This method allowed us to obtain both top and side topographies of the pillars.

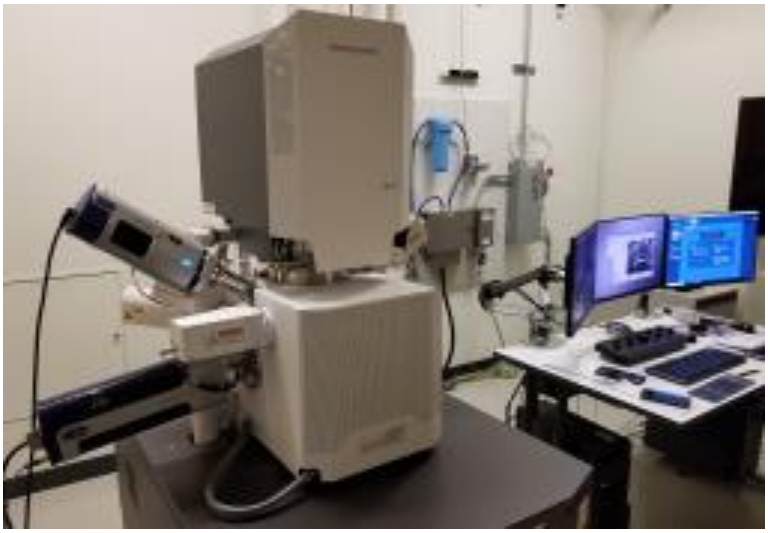

Figure 13. Apparatus set up of the EBSD SEM located in the MAF.

3. Results & Discussion

The following section will entail results and discussion from our printability and micro compression studies. Pillar printability is first evaluated through SEM and LSM to determine optimized printing parameters for each pillar diameter size of 10um, 1um, 600nm, 500nm, 400nm, and 300nm with an aspect ratio of 3. The post-processing study is then discussed to outline the process resulting in standing pillars with minimal deformation. Next, Raman spectroscopy is assessed to find the DOP of bulk and pillar samples. Following the section on

printability, analysis of the pillar micro-compression tests is conducted to determine the mechanical properties and size effects between pure polymer and composite pillars.

3.1. Optimizing Printability

3.1.1. Visual Inspection via SEM and LSM

To begin, we conducted parameter sweeps to determine the optimal set of laser power and scan speed parameters. SEM and LSM were used to image the corresponding pillars for qualitative evaluation. Table 4 summarizes the optimal parameters specified from these sweeps. Shown in Figure 14 are SEM images of optimally printed and post-processed 1um, 600nm, 500nm, 400nm, and 300nm pillars. For 10um pillars, SEM images are seen in Figures 17c and 17d.

Table 4: Optimal laser power and scan speed for each pillar type.

		Pure Polymer		Composite	
Pillar Diameter	**Writing Mode**	**Laser Power [%]**	**Scan Speed [µm/s]**	**Laser Power [%]**	**Scan Speed [µm/s]**
10um	**Galvo**	66	5400	58	5400
1um	**Piezo**	100	300	92	200
600nm	**Piezo**	100	260	100	225
500nm	**Piezo**	95	200	100	200
400nm	**Piezo**	100	260	100	150
300nm	**Piezo**	100	375	100	225

Observations noted during these sweeps were increasing laser power and decreasing scan speed led to high concentrations of energy resulting in mini-explosions and severe defects of the pillar structures. Therefore, the goal was to determine a balance between the two parameters enabling the fabrication of standing pillars with none or minimal distortions. Regarding the behavior of the materials themselves, the CNTs were expected to act as a catalysts [46]. We anticipated a reduction in laser power or increase in scan speed for the composite pillars, but results

showed similar parameters to the pure polymer pillars. The 10um pillar parameters produced expected results, whereas the smaller pillar behavior deviated from the expected. One possible explanation is that CNTs may uptake some of the supplied laser power for internal structural conformations thereby competing with the polymer/initiator at the smaller polymerization volumes. Parameter sweeps were conducted only once per wafer. Future work is needed to quantify the dosage-dependent polymerization thresholds as a function of polymerization volume.

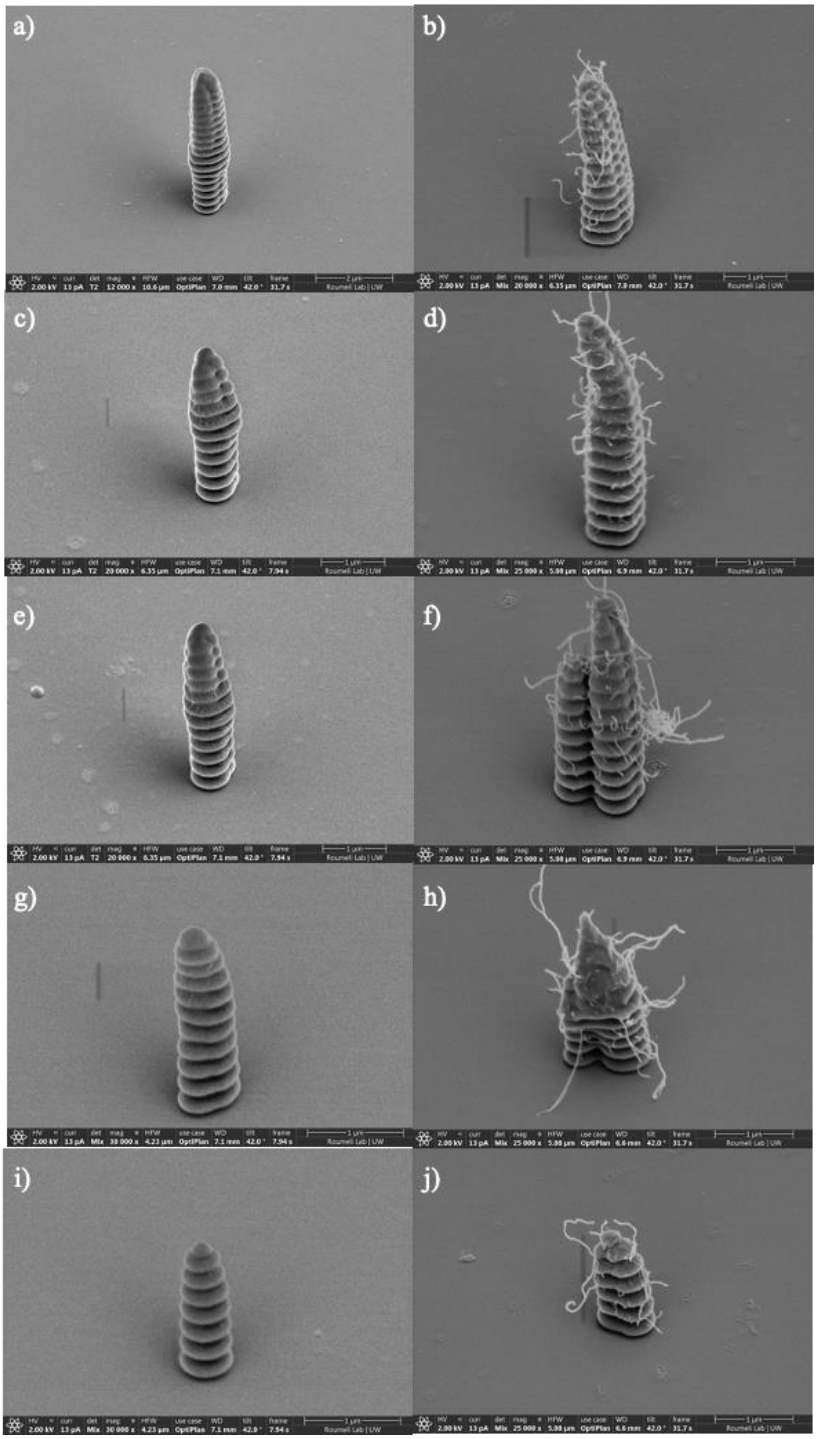

Figure 14. Pure Polymer SEM images of (a) 1um, (c) 600nm, (e) 500nm, (g) 400nm, and (i) 300nm pillars. Composite SEM images of (b) 1um, (d) 600nm, (f) 500nm, (h) 400nm, and (j) 300nm pillars. Pillars were fabricated using the ideal parameters determined in Table 3 and were post-processed as outlined in Section 3.1.2.

3.1.2. Post-Processing Effects

The post-processing study demonstrated that the UV curing steps for both the parallel with development and post-CPD had ideal standing pillars, as seen in Table 4. On the other hand, most air-dried pillars were collapsed and distorted, most likely due to stronger capillary forces during the dry. The finalized post-processing procedure combined the UV exposure during development and post-CPD. By incorporating more instances of UV exposure, the goal was to allow more crosslinking of the polymer and increase the DOP, thereby improving the structural stability of the pillars. Additionally, input from process engineers at the WNF requested to extend the development time of all samples going into the CPD system. This increased duration minimizes the likelihood of contamination within the drying chamber and reduces filter changeout frequency. The post-processing procedure is then finalized as 5 minutes in PGMEA solution, 5 minutes in IPA, 10minutes in Ultra-Pure IPA, Ultra-Pure IPA, and simultaneous UV curing for 30seconds on and off for a total of 5 minutes, dried in the CPD, and then exposed to UV light for 5 minutes.

Table 5: Post-processing results of pure polymer and composite.

Post-Process	Pure Polymer	Composite
Pillars CPDed, No Curing	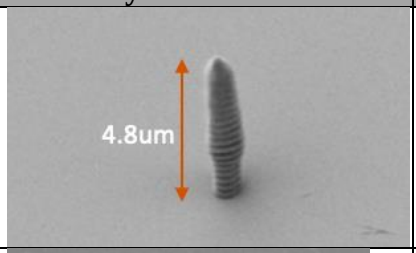	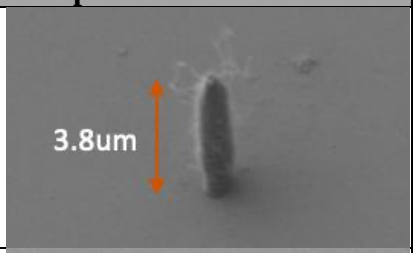
Pillars UV Illuminated during Pure IPA step + CPDed	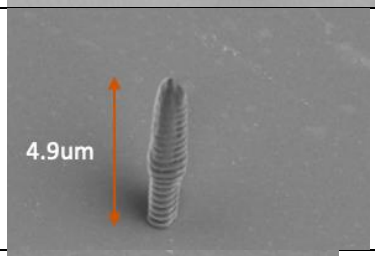	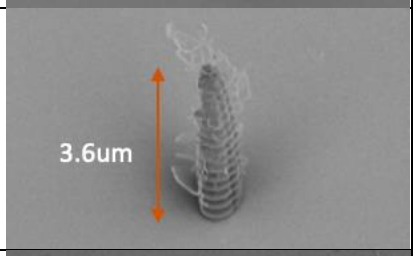
Pillars UV illuminated during Pure IPA step before air drying		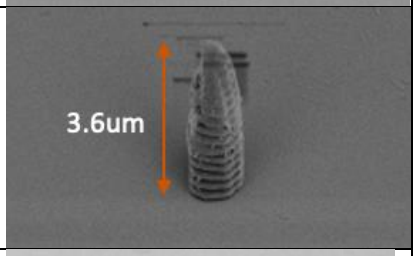
Pillars are air dried	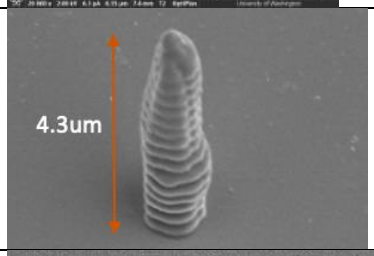	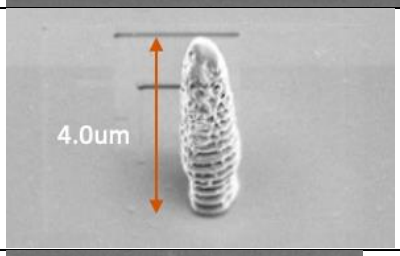
Pillars CPDed + UV post cure (300 sec)	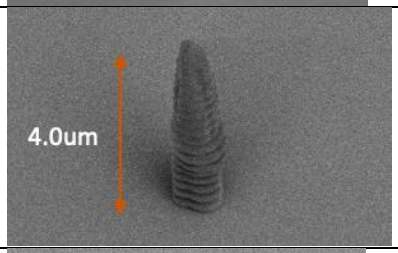	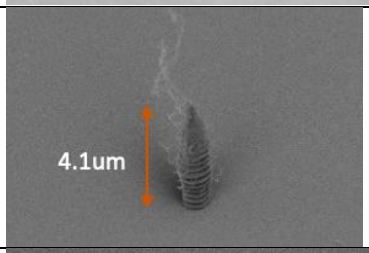
Pillars CPDed + UV post cure (60 sec)	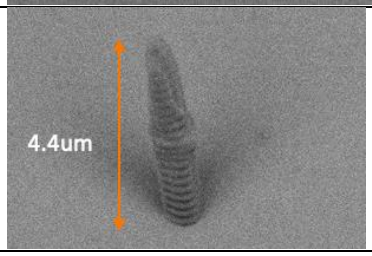	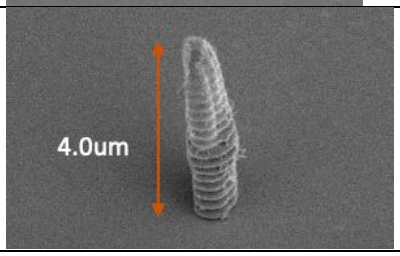

3.1.3. Raman Spectroscopy

Raman spectroscopy was performed to determine the degree of polymerization of 10um pillars and bulk thin film samples from both pure polymer and composite materials. The 10um pillars underwent 0-, 1-, 10-, 30-, and 60-minute post UV exposure times after CPD drying. The bulk thin film sample underwent 1-, 5-, 30-, and 60- minute UV exposure times. These film samples were prepared by applying a drop of resin on a 6x6mm^2 silicon wafer and then spread manually with a razor blade. Post-processing for the bulk films after exposure was 5 minutes in PGMEA, 5 minutes in IPA, and then air-dried. Figure 15 shows an example of the film. Due to their signals not being strong enough for measurement, we were unable to determine the degree of polymerization for 1um diameter and smaller pillars.

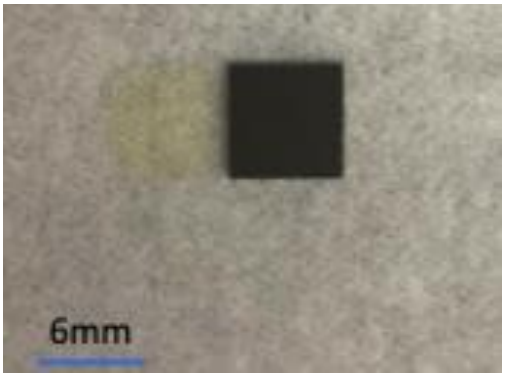

Figure 15. Pure polymer bulk film sample (left) next to a 6x6mm^2 silicon substrate.

Figure 16 shows the distribution of the degree of polymerization from 10um pillar and bulk samples. Here, bulk demonstrated higher polymerization values than the 10um pillars for both pure polymer and composite materials. Across all exposure times, pure polymer bulk film ranged between 41.0%-60.76%, whereas the 10um pillars were in a range of 26.0%-38.1%. For composite, bulk filmed valued in the range of 40.6%-52.3% and 10um pillars was 26.2%-39.7%. The difference in performance between bulk and pillar samples may be due to different

polymerization volume (size-related effect). In addition, the type of polymerization undergone by these two samples was different. The pillars underwent 2PP, and the bulk film polymerized via UV light. These degrees of polymerization ranges are also similar to that those of other acrylic-based resins [44], [45].

Comparing the materials, both pure polymer and composite yielded similar DOPs. Though, the pure polymer bulk sample achieved the highest value of polymerization of 60.76% at 5 minutes of UV curing. Its performance was then reduced for 30-minute and 60-minute curing times. Such variations may be related to inconsistencies due to the manual sample preparation that includes sample/UV lamp relative positioning, which influence the distance and thus, delivered dosage, as well as layer thickness variations which may cause a spatial distribution in the degree of polymerization. Polymerization of thinner areas would occur much easier than thicker areas due to less material and depth the light would have to travel. From this, variation is likely to occur within the Raman spectroscopy measurements. However, regarding the 10um pillars, the DOP remains unaffected from post-curing time, indicating that the materials have already saturated crosslinking before the final post-curing step. This can be related to the fact that all pillars are already pre-exposed for 5 minutes to UV during their development, so it is likely that they reach their saturation degree during that step. Comparisons between the DOP of pillars with and without that exposure step are required to confirm this conclusion.

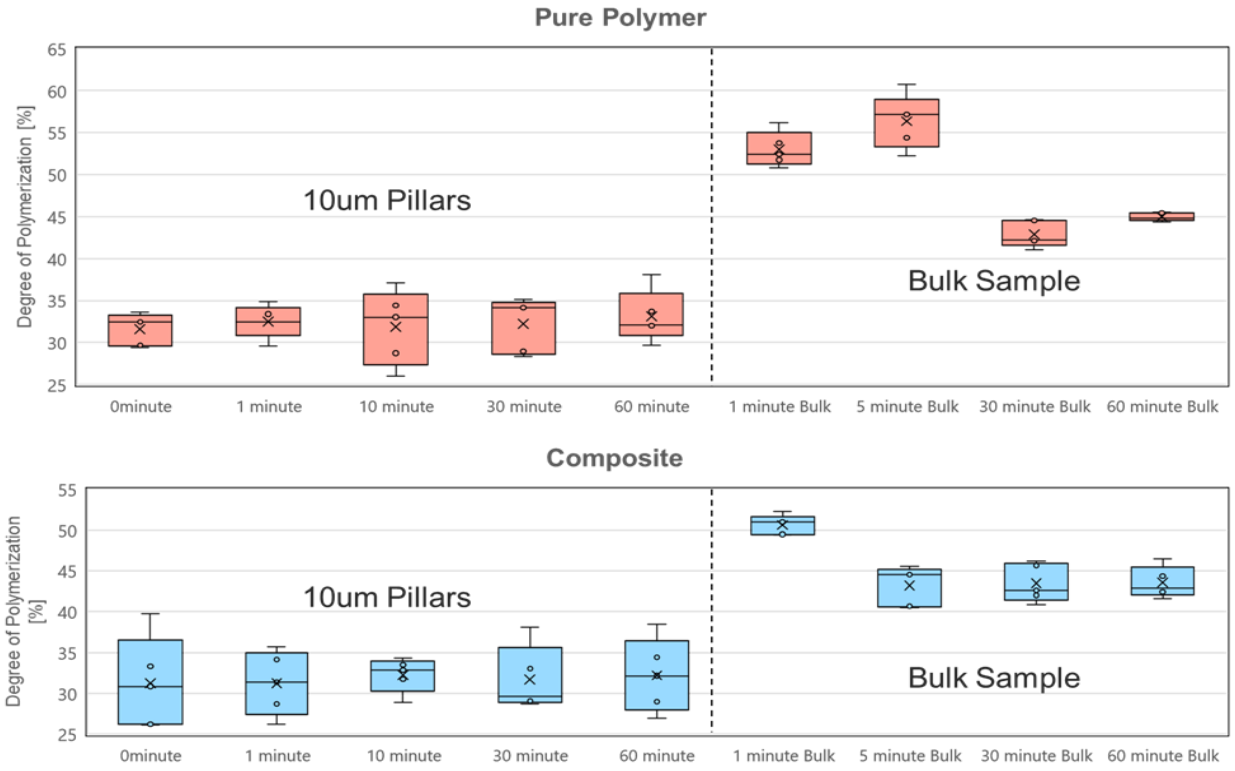

Figure 16. Degree of polymerization for 10um diameter pillars and bulk film samples with different UV exposure times. Pure polymer (top) and composite (bottom) are shown.

3.2. Mechanical Properties

The following section discusses the mechanical properties of our samples obtained through micro-compression and nanoindentation testing. As mentioned previously in Section 2.3.2, 10um pillars were tested differently than compared to smaller pillars due to resolution of data obtained. For 10um, a 50x100um^2 flat punch tip was used with max force of 2000uN whereas smaller pillars used a spherical tip with max force of 200uN.

3.2.1. 10um Diameter Pillars and Nanoindentation of Bulk Films

10um diameter pillars were first mechanically tested and force-displacement plots were obtained shown in Figures 17a and 17b. As noted in Section 2.3.2, stiffness and yield point were obtained from the raw force-displacement curves. These values were then converted to young's modulus and strength, as would be seen on a stress-strain curve. Calculating the average of these values resulted in Young's modulus values of 454.2 MPa and 484.83 MPa for pure polymer and composite 10um pillars, respectively. The composite material performing higher than the pure polymer aligns with other works where the CNTs were utilized as a strengthening filler [2]. The effect is smaller in the strength as values of 20.91 MPa and 21.44 MPa for pure polymer were obtained and composite, respectively.

Between the two materials, data distribution is also an important aspect to consider. Figures 17c and 17d show a significant magnitude of distribution compared to that of pure polymer. It is also seen that a few of the composite 10um pillars performed in the same range as the pure polymer. This suggests a potentially non-uniform CNT distribution in the resin.

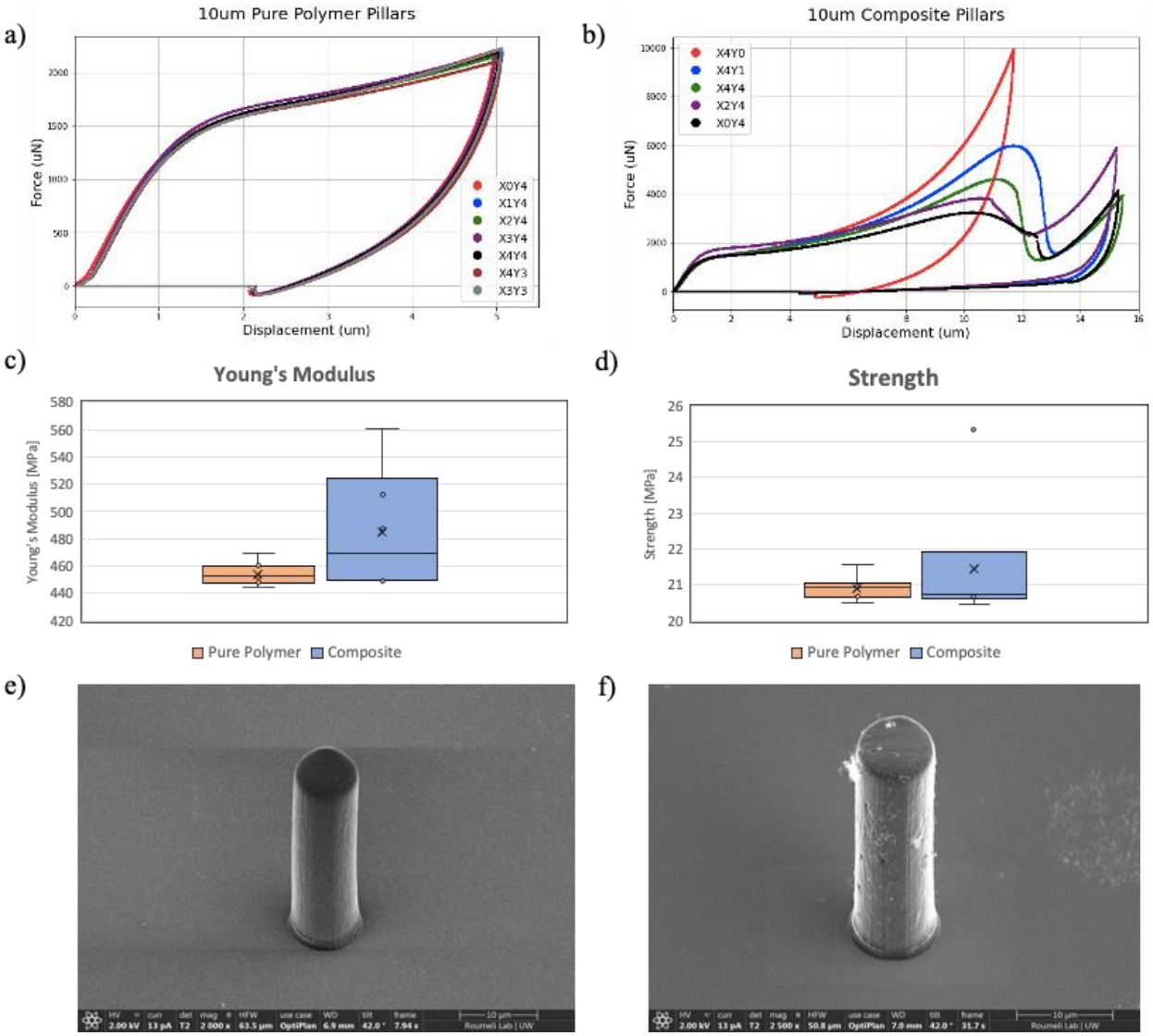

Figure 17. Force-Displacement plots of 10um pillars for (a) pure polymer and (b) composite with pillar location identified. Plots of (a) Young's Modulus and (b) Strength values for 10um pure polymer and composite pillars. SEM images of (c) pure polymer and (d) composite 10um diameter pillars.

Nanoindentation was also performed on bulk films allowing the measurement of a reduced modulus and hardness for pure polymer and composite materials. Using a diamond Berkovich tip of 2000uN max force, in the same micromechanical system used for compression tests, and a load

rate of 0.1um/s, nanoindentation was performed as a 10x10 matrix with a spacing of 2um between each probing point. These films underwent 10 minutes of UV curing. For the pure polymer film, median modulus and median hardness were 3031.1 ±531.0 MPa and 142.4 ±34.1 MPa, respectively. The composite film showed a median modulus and median hardness of 2927.4 ±512.5 MPa and 126.5 ±31.0 MPa, respectively. These results clearly demonstrate that the composite and polymer have no difference in their bulk macroscopic performance. This is in agreement with prior results [38] which show that at such low concentrations (here we use 0.004 wt%) CNTs do not reinforce the performance of the bulk polymer, but only when a microstructure is introduced through 2PP influences of the filler start becoming apparent.

3.2.2. 1um, 600nm, 500nm, 400nm, and 300nm Diameter Pillars

From the three methods outlined in Section 2.3.2, geometric volume conservation assumptions will be used to determine Young's moduli and strength values of our pillars as it best represents the geometry of the pillars. In Figure 18, plots of mechanical behavior against apparent diameter using these methods are presented. Here, a moving average is applied to the data to visualize the trends. Values for both mechanical properties appear to be decreasing as pillar diameter increases. The only exceptions are for the composite Young's Moduli values using the methods of no volume conservation and base radius. The difference could be attributed to how these two methods misrepresent the cross-sectional areas of the smaller pillars. The base radius assumptions to calculate the cross-sectional area resulted in an overestimation of the area due to it ignoring the conical-like and slimming of the pillar moving from bottom to top. This is seen in the SEM images for the composite pillars in Figure 14. As for the method using no volume conservation, a conical shape is assumed but it neglects the deformation of the pillar during

compression. Therefore, the volume conservation method will be applied to evaluate these pure polymer and composite pillars.

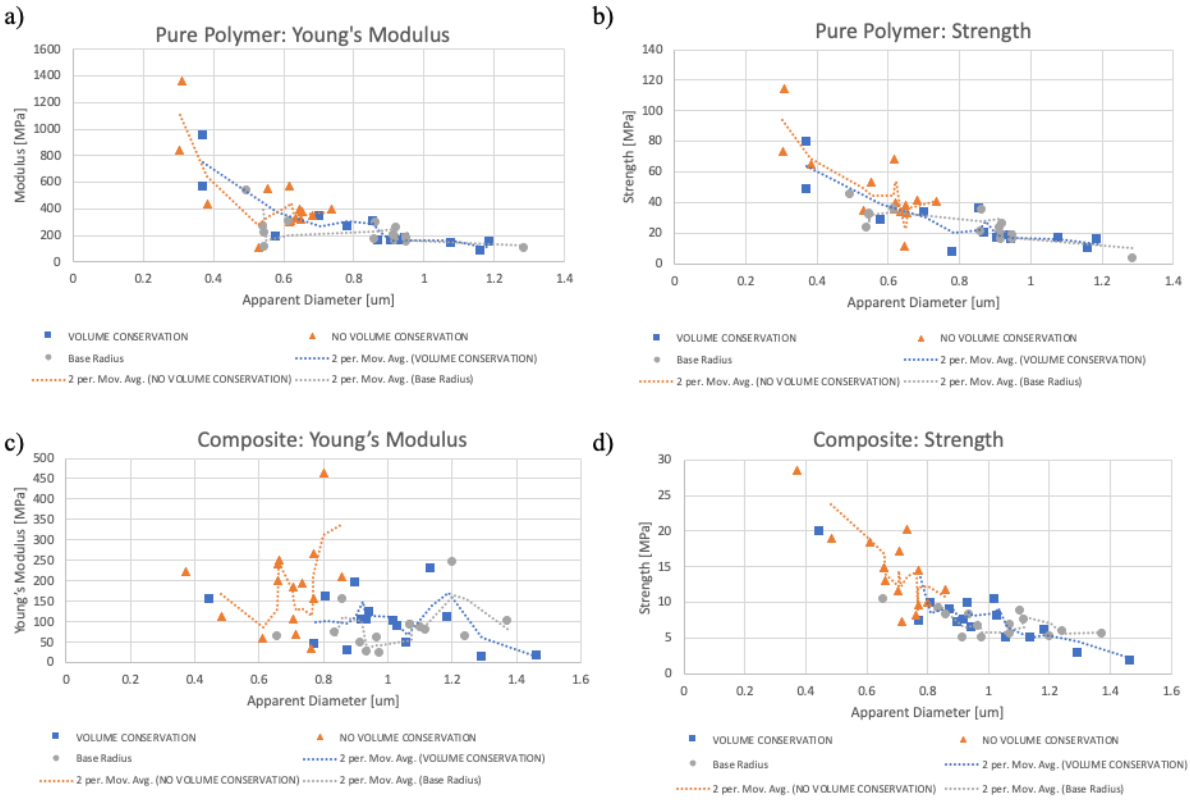

Figure 18. Plots of Young's Modulus and Strength for pure polymer and composite materials using methods of volume conservation, no volume conservation, and base radius to define pillar geometries.

3.2.2.1. Pure Polymer Pillars

Examining the plots of the pure polymer in Figure 19, both Young's Modulus and Strength demonstrate an increase with decreasing apparent pillar diameter ($\bar{d}$). As mentioned, the apparent diameter is the circular diameter that was back calculated from the elliptical top-view SEM images. A power law fit was applied to the data to observe the relationship between these mechanical

properties and micro- and nano-scaled pillars. For Young's Modulus and Strength, the best fits are defined as:

$$E = 148.42\bar{d}^{-1.62} \quad (11)$$

$$\sigma = 17.9\bar{d}^{-1.27} \quad (12)$$

Comparing the pure polymer pillars of smaller diameter to that of the 10um diameter pillars, we see a significant increase in mechanical properties from the pillar with the smallest apparent diameter. The average value of Young's Modulus and Strength for the 10um pillars are 454.2 MPa and 20.91 MPa, respectively. Now observing Figure 19, the smallest diameter calculated of 0.37um shows a Young's Modulus and Strength of 945.02 MPa and 79.53 MPa, respectively. This double and quadrupling of values could be attributed to the size effects influencing mechanical properties. In theory, the reason for such enhancement of mechanical properties at a smaller scale is due to differences in the macromolecular packing (polymer confinement): It has been shown that when polymers are nanoconfined, which in our case would be more pronounced for the smaller sample sizes, their macromolecular arrangement is significantly altered, affecting their glass transition temperature as well as their mechanical properties [47]. Specifically, a stiffening effect has been experimentally observed as a result of confining amorphous polymers in nanosized domains. Our data confirm these observations as a stiffening and strengthening is observed as the pillar size decreases.

While a power-law trend is applied to the smaller pillars, this trend wouldn't apply if 10um pillar data were included, suggesting that a size-depended behavior is manifested in the submicron scale. Another factor to account for is the geometric differences of the pillars themselves. 10um

diameter pillars appear to be ideally cylindrical, and features such as height and cross-sectional area were easily determined. As for the smaller pillars, they were more conical in shape. This geometrical imperfection called for more round-about calculations to determine their mechanical properties. In fact, if the pillars are not cylindrical with a flat cross-section perpendicular to the indenter's punch, we may be probing bending and effects such as buckling may occur, violating the assumptions of a straight column compression. In addition, the topography of the smaller pillars is not smooth. As seen in Figure 14, the shape appears closer to disks stacked on top of each other. Capillary forces may cause the series of ridges seen on the side during the drying process. Another reason for such ridges could be from standing waves, potentially arising from the laser source's incident waves being reflected off the silicon substrate [48]. To better compare these structures, consistent geometries will be needed.

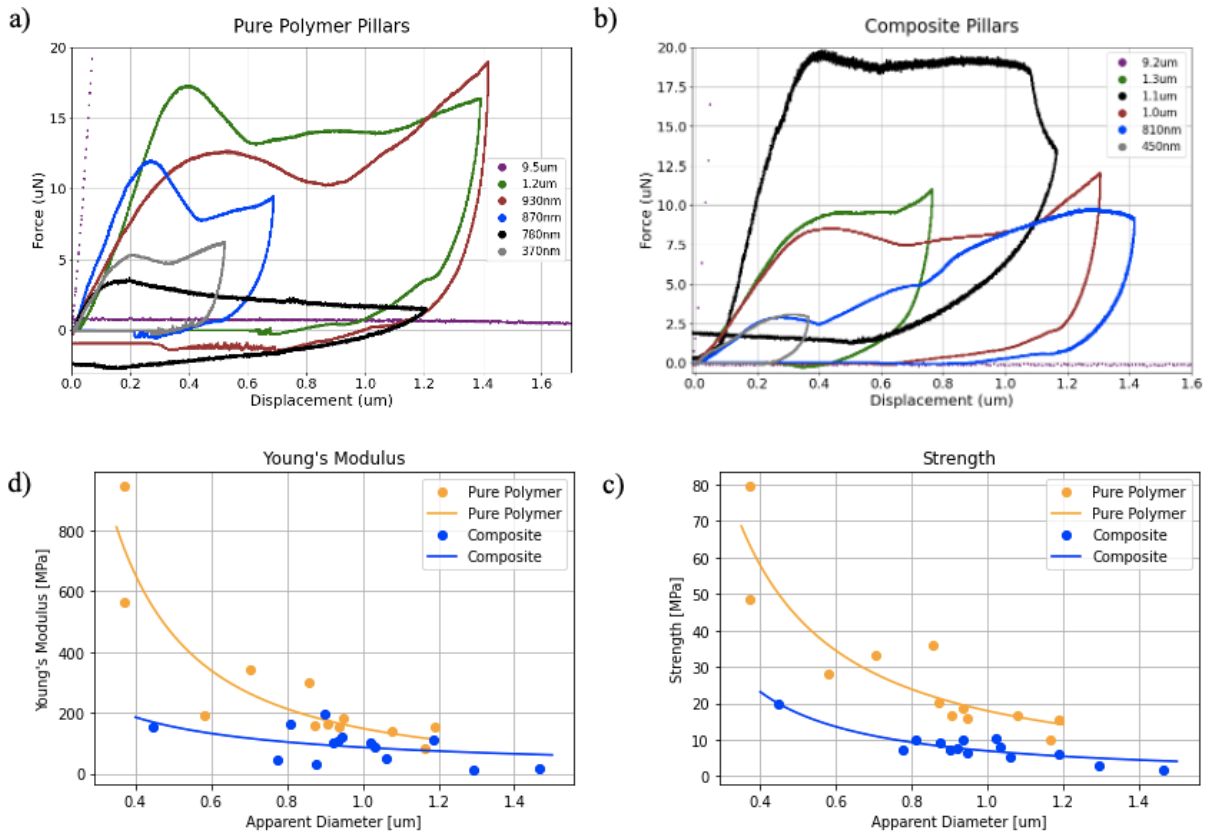

Figure 19. Force-Displacement plots of (a) pure polymer and (b)composite pillars. Plots of (c) Young's Modulus and (d) Strength against apparent diameter for pure polymer and composite pillars. The lines represent scaling laws applied to observe size effects.

3.2.2.2. Composite pillars

Following what was done for the pure polymer pillars, the mechanical properties of composite pillars were measured. The initial hypothesis was that the CNTs would be used as reinforcement to further improve mechanical properties of the structures. Especially as the CNTs used are functionalized, studies have shown it would lead to better dispersion and high interfacial adhesion between the CNTs and polymer matrix resulting in enhanced mechanical characteristics [49], [50]. Our measurements cannot confirm this hypothesis. The composite pillars underperform compared to the pure polymer. Their power law fits for Young's Modulus and Strength are outlined as:

$$E = 85.95\bar{d}^{-0.84} \quad (13)$$

$$\sigma = 6.9\bar{d}^{-1.32} \quad (14)$$

Two possible reasons can explain the observed underperformance of the composite pillars. First, the geometries of the tested pillars. SEM observations of the microstructures of pure polymer versus composite, provided in Figure 14, demonstrate a lack of consistency in terms of pillar shape for the composites. Although the printing script was set to fabricate single pillars, some composite pillars resulted in two pillars attached to each other. There is uncertainty as to why this occurred as the same STL file was used for both pure polymer and composite of the same diameters. The only differences were the laser power and scan speed inputs. The presence of CNTs affects the

polymerization volume, possibly hindering the termination reactions, thereby leading to larger solidified voxels, deviating from the intended shape. Hence, when calculating the mechanical properties, the pillars exhibiting a “twin-pillar” effect would have a larger cross-sectional area. When applying Equations (2) and (3), this increase in area lowers the values for Young’s Modulus and Strength with increasing cross-sectional area. This effect did not appear for all pillars within the final set for mechanical testing, but rather a subset of them. A proposed solution would be to inspect the pillars individually in SEM before mechanical testing. These “twin pillars” were not identified until after mechanical testing and observing under the SEM after surface coating was deposited.

The second, less likely reason for the composite pillars' lower performance could be the non-uniform CNTs distribution. As mentioned previously, the dispersion of the CNTs may not have been uniform, resulting in a inhomogeneous distribution of the CNTs exposed for each pillar printed. However, as seen in Figure 14, the composite pillars contain CNTs, which are protruding out in different directions, without providing evidence for a distinct difference in the CNT distribution. Yet we do observe a lack of controlled directionality of the CNTs, as was suggested by prior studies [30], [51]. Figure 14f also shows a sign of CNT bundling rather than individual CNT distribution, which indicates imperfect dispersion. Such entanglements and agglomerations seen likely lead to insufficient bonding at the matrix-filler interface and poor mechanical properties. Solutions to explore are longer homogenizing times for the mixtures or the use of more amount of stabilization or functionalization agents. Another area of future interest is also the alignment of CNTs. As with conventional carbon fiber composites, alignment is crucial when optimizing the properties of the fibers. Mechanical properties are more pronounced along fiber

direction (longitudinal) than the perpendicular direction (transverse) [52]. Controlling the CNT direction would likely enable the fine tuning of mechanical properties.

Size effects can somewhat be seen with the composite pillars in Figure 19. While not as prominent as the pure polymer, a power-law fit can still be applied, as mentioned previously. It is not conclusive that size effects are playing a role in this trend because of other significant factors like overall pillar shape, and less significantly, CNT distribution, but similarly to the pure polymer pillars, future work will need to investigate how to obtain better consistency across pillar geometries.

4. Conclusions and Future Work

Our work investigated polymer and nanocomposite pillars' printability and their resulting mechanical properties. In terms of printability, parameter sweeps were conducted to determine optimal parameters of scan speed and laser power. Parallel with the parameter sweeps for 1um diameter pillars, a post-processing study was done to ensure standing pillars with the best geometry. Results showed that the addition of UV exposure steps and drying with CPD resulted in the best-seen pillars.

Regarding mechanical testing of the pillars, 10um pillars were first investigated, producing expected higher performance of the nanocomposite over pure polymer materials. Though, it was seen that a wider spread of Young's Moduli and strengths was obtained for the nanocomposites. Nanoindentation of the bulk film materials was also performed. Unlike the 10um pillars, results showed no difference in the bulk mechanical properties of composite material compared to the pure polymer. This is in agreement with our hypothesis that effects from introducing ultra-low

amounts of CNTs (here we use 0.004 wt%) appear only when microstructures are fabricated and not in bulk.

To further explore the size effects, pillar samples with targeted diameters of 1um, 600nm, 500nm, 400nm, and 300nm were mechanically tested. For both types of pillars, a power law was fitted onto both. Unlike the larger 10um pillars, the nanocomposite pillars did now allow systematic compression due to significant deviations from the expected cylindrical shape in presence of the CNTs. Thus, the deviation of the testing conditions from a single beam in compression, potentially skew the results, that do not show any improvement in presence of the filler. To better understand and evaluate these effects, a different printing geometry that would prevent deviations from cylindrical shape and ensure that the tested beam would be under pure compression need to be developed.

In addition, sample preparation to reduce standing wave effects may be a route to pursue. Particularly the usage of anti-reflective coatings or just a non-reflective substrate could be beneficial. Obtaining more data will also be important to improve our understanding of these pillar mechanical behavior and size effects. As noted, the results section, data below 0.8um in diameters were scarce. These repetitions are insufficient to draw a comprehensive conclusion regarding pillar behavior and size effects. Finally, CNT content can be a path to explore and its effects on mechanical properties and printability.

5. References

[1] N. Nanoscribe, “3D Printing using Two Photon Polymerization (2PP).” [Online]. Available: https://support.nanoscribe.com/hc/en-gb/articles/360008908273-3D-Printing-using-Two-Photon-Polymerization-2PP-

[2] Y. Liu, W. Xiong, L. J. Jiang, Y. S. Zhou, and Y. F. Lu, “Precise 3D printing of micro/nanostructures using highly conductive carbon nanotube-thiol-acrylate composites,” San Francisco, California, United States, Apr. 2016, p. 973808. doi: 10.1117/12.2214862.

[3] J. Purtov, A. Verch, P. Rogin, and R. Hensel, “Improved development procedure to enhance the stability of microstructures created by two-photon polymerization,” *Microelectron. Eng.*, vol. 194, pp. 45–50, Jul. 2018, doi: 10.1016/j.mee.2018.03.009.

[4] A. Sigma, “Di(trimethylolpropane) tetraacrylate.” [Online]. Available: https://www.sigmaaldrich.com/US/en/product/aldrich/408360

[5] A. Sigma, “2-Benzyl-2-(dimethylamino)-4′-morpholinobutyrophenone.” [Online]. Available: https://www.sigmaaldrich.com/US/en/product/aldrich/405647

[6] S. C. Tjong, “Structural and mechanical properties of polymer nanocomposites,” *Mater. Sci. Eng. R Rep.*, vol. 53, no. 3–4, pp. 73–197, Aug. 2006, doi: 10.1016/j.mser.2006.06.001.

[7] P. M. Ajayan, L. S. Schadler, and P. V. Braun, *Nanocomposite science and technology*. Weinheim: Wiley-VCH, 2003.

[8] J. K. Watson and K. M. B. Taminger, “A decision-support model for selecting additive manufacturing versus subtractive manufacturing based on energy consumption,” *J. Clean. Prod.*, vol. 176, pp. 1316–1322, Mar. 2018, doi: 10.1016/j.jclepro.2015.12.009.

[9] H. Wu *et al.*, “Recent developments in polymers/polymer nanocomposites for additive manufacturing,” *Prog. Mater. Sci.*, vol. 111, p. 100638, Jun. 2020, doi: 10.1016/j.pmatsci.2020.100638.

[10] H. Qian, E. S. Greenhalgh, M. S. P. Shaffer, and A. Bismarck, “Carbon nanotube-based hierarchical composites: a review,” *J. Mater. Chem.*, vol. 20, no. 23, p. 4751, 2010, doi: 10.1039/c000041h.

[11] M. Moniruzzaman and K. I. Winey, “Polymer Nanocomposites Containing Carbon Nanotubes,” *Macromolecules*, vol. 39, no. 16, pp. 5194–5205, Aug. 2006, doi: 10.1021/ma060733p.

[12] M.-F. Yu, B. S. Files, S. Arepalli, and R. S. Ruoff, “Tensile Loading of Ropes of Single Wall Carbon Nanotubes and their Mechanical Properties,” *Phys. Rev. Lett.*, vol. 84, no. 24, pp. 5552–5555, Jun. 2000, doi: 10.1103/PhysRevLett.84.5552.

[13] N. Grossiord, J. Loos, O. Regev, and C. E. Koning, “Toolbox for Dispersing Carbon Nanotubes into Polymers To Get Conductive Nanocomposites,” *Chem. Mater.*, vol. 18, no. 5, pp. 1089–1099, Mar. 2006, doi: 10.1021/cm051881h.

[14] D. Qian, E. C. Dickey, R. Andrews, and T. Rantell, “Load transfer and deformation mechanisms in carbon nanotube-polystyrene composites,” *Appl. Phys. Lett.*, vol. 76, no. 20, pp. 2868–2870, May 2000, doi: 10.1063/1.126500.

[15] X. Xie, Y. Mai, and X. Zhou, “Dispersion and alignment of carbon nanotubes in polymer matrix: A review,” *Mater. Sci. Eng. R Rep.*, vol. 49, no. 4, pp. 89–112, May 2005, doi: 10.1016/j.mser.2005.04.002.

[16] S. Dul, L. Fambri, and A. Pegoretti, “Filaments Production and Fused Deposition Modelling of ABS/Carbon Nanotubes Composites,” *Nanomaterials*, vol. 8, no. 1, p. 49, Jan. 2018, doi: 10.3390/nano8010049.

[17] I.-Y. Jeon, D. Wook, N. Ashok, and J.-B. Baek, “Functionalization of Carbon Nanotubes,” in *Carbon Nanotubes - Polymer Nanocomposites*, S. Yellampalli, Ed. InTech, 2011. doi: 10.5772/18396.

[18] J. Z. Manapat, Q. Chen, P. Ye, and R. C. Advincula, “3D Printing of Polymer Nanocomposites via Stereolithography,” *Macromol. Mater. Eng.*, vol. 302, no. 9, p. 1600553, Sep. 2017, doi: 10.1002/mame.201600553.

[19] K. Kurselis, R. Kiyan, V. N. Bagratashvili, V. K. Popov, and B. N. Chichkov, “3D fabrication of all-polymer conductive microstructures by two photon polymerization,” *Opt. Express*, vol. 21, no. 25, p. 31029, Dec. 2013, doi: 10.1364/OE.21.031029.

[20] J. Bauer, L. R. Meza, T. A. Schaedler, R. Schwaiger, X. Zheng, and L. Valdevit, “Nanolattices: An Emerging Class of Mechanical Metamaterials,” *Adv. Mater.*, vol. 29, no. 40, p. 1701850, Oct. 2017, doi: 10.1002/adma.201701850.

[21] L. R. Meza, “Design, Fabrication, and Mechanical Property Analysis of 3D Nanoarchitected Materials,” p. 151.

[22] L. R. Meza, S. Das, and J. R. Greer, “Strong, lightweight, and recoverable three-dimensional ceramic nanolattices,” *Science*, vol. 345, no. 6202, pp. 1322–1326, Sep. 2014, doi: 10.1126/science.1255908.

[23] J. B. Müller, “Exploring the Mechanisms of Three-Dimensional Direct Laser Writing by Multi-Photon Polymerization,” p. 161.

[24] S. Kawata, H.-B. Sun, T. Tanaka, and K. Takada, “Finer features for functional microdevices,” *Nature*, vol. 412, no. 6848, pp. 697–698, Aug. 2001, doi: 10.1038/35089130.

[25] L. J. Jiang, S. Maruo, R. Osellame, W. Xiong, J. H. Campbell, and Y. F. Lu, “Femtosecond laser direct writing in transparent materials based on nonlinear absorption,” *MRS Bull.*, vol. 41, no. 12, pp. 975–983, Dec. 2016, doi: 10.1557/mrs.2016.272.

[26] S. C. Ligon, R. Liska, J. Stampfl, M. Gurr, and R. Mülhaupt, “Polymers for 3D Printing and Customized Additive Manufacturing,” *Chem. Rev.*, vol. 117, no. 15, pp. 10212–10290, Aug. 2017, doi: 10.1021/acs.chemrev.7b00074.

[27] A. Bauhofer, “Multiscale Effects of Photochemical Shrinkage in Direct Laser Writing,” ETH Zurich, 2019. doi: 10.3929/ETHZ-B-000339159.

[28] J. R. Fried, *Polymer science and technology*, Third edition. Upper Saddle River, NJ: Prentice Hall, 2014.

[29] L. Chen *et al.*, “Development of Direct-Laser-Printable Light-Powered Nanocomposites,” *ACS Appl. Mater. Interfaces*, vol. 11, no. 21, pp. 19541–19553, May 2019, doi: 10.1021/acsami.9b05871.

[30] W. Xiong *et al.*, “Laser-Directed Assembly of Aligned Carbon Nanotubes in Three Dimensions for Multifunctional Device Fabrication,” *Adv. Mater.*, vol. 28, no. 10, pp. 2002–2009, Mar. 2016, doi: 10.1002/adma.201505516.

[31] M. Carlotti and V. Mattoli, “Functional Materials for Two-Photon Polymerization in Microfabrication,” *Small*, vol. 15, no. 40, p. 1902687, Oct. 2019, doi: 10.1002/smll.201902687.

[32] K. Masui *et al.*, “Laser fabrication of Au nanorod aggregates microstructures assisted by two-photon polymerization,” *Opt. Express*, vol. 19, no. 23, p. 22786, Nov. 2011, doi: 10.1364/OE.19.022786.

[33] Y. Lin and J. Xu, “Microstructures Fabricated by Two-Photon Polymerization and Their Remote Manipulation Techniques: Toward 3D Printing of Micromachines,” *Adv. Opt. Mater.*, vol. 6, no. 8, p. 1701359, Apr. 2018, doi: 10.1002/adom.201701359.

[34] J. Purtov, P. Rogin, A. Verch, V. E. Johansen, and R. Hensel, “Nanopillar Diffraction Gratings by Two-Photon Lithography,” *Nanomaterials*, vol. 9, no. 10, p. 1495, Oct. 2019, doi: 10.3390/nano9101495.

[35] “Physical, Thermal, and Mechanical Properties of Polymers,” in *Biosurfaces*, Hoboken, NJ, USA: John Wiley & Sons, Inc, 2015, pp. 329–344. doi: 10.1002/9781118950623.app1.

[36] J. Bauer, A. Guell Izard, Y. Zhang, T. Baldacchini, and L. Valdevit, “Programmable Mechanical Properties of Two-Photon Polymerized Materials: From Nanowires to Bulk,” *Adv. Mater. Technol.*, vol. 4, no. 9, p. 1900146, Sep. 2019, doi: 10.1002/admt.201900146.

[37] H. Namatsu, K. Yamazaki, and K. Kurihara, “Supercritical drying for nanostructure fabrication without pattern collapse,” *Microelectron. Eng.*, vol. 46, no. 1–4, pp. 129–132, May 1999, doi: 10.1016/S0167-9317(99)00033-7.

[38] E. Roumeli, S. Krodel, N. Nianas, and C. Daraio, “Size-dependent mechanical reinforcement in direct laser written CNT-composite lattices”.

[39] “Multi Walled Carbon Nanotubes.” [Online]. Available: https://www.cheaptubes.com/product-category/multi-walled-carbon-nanotubes/

[40] J. Mao, Y. Wang, J. Zhu, J. Yu, and Z. Hu, “Thiol functionalized carbon nanotubes: Synthesis by sulfur chemistry and their multi-purpose applications,” *Appl. Surf. Sci.*, vol. 447, pp. 235–243, Jul. 2018, doi: 10.1016/j.apsusc.2018.03.188.

[41] J. Wang, J. Lian, J. Greer, W. Nix, and K. Kim, “Size effect in contact compression of nano- and microscale pyramid structures,” *Acta Mater.*, vol. 54, no. 15, pp. 3973–3982, Sep. 2006, doi: 10.1016/j.actamat.2006.04.030.

[42] “Nanoscribe Photonic Professional (GT).” University of Pittsburgh.

[43] N. Nanoscribe, “Printing Modes.”

[44] J. S. Oakdale, J. Ye, W. L. Smith, and J. Biener, “Post-print UV curing method for improving the mechanical properties of prototypes derived from two-photon lithography,” *Opt. Express*, vol. 24, no. 24, p. 27077, Nov. 2016, doi: 10.1364/OE.24.027077.

[45] L. J. Jiang *et al.*, “Two-photon polymerization: investigation of chemical and mechanical properties of resins using Raman microspectroscopy,” *Opt. Lett.*, vol. 39, no. 10, p. 3034, May 2014, doi: 10.1364/OL.39.003034.

[46] N. M. Nurazzi *et al.*, “Mechanical Performance and Applications of CNTs Reinforced Polymer Composites—A Review,” *Nanomaterials*, vol. 11, no. 9, p. 2186, Aug. 2021, doi: 10.3390/nano11092186.

[47] X. Cheng, K. W. Putz, C. D. Wood, and L. C. Brinson, “Characterization of Local Elastic Modulus in Confined Polymer Films via AFM Indentation,” *Macromol. Rapid Commun.*, vol. 36, no. 4, pp. 391–397, Feb. 2015, doi: 10.1002/marc.201400487.

[48] C. A. Mack, *Field Guide to Optical Lithography*. 1000 20th Street, Bellingham, WA 98227-0010 USA: SPIE, 2006. doi: 10.1117/3.665802.

[49] G.-X. Chen, H.-S. Kim, B. H. Park, and J.-S. Yoon, “Multi-walled carbon nanotubes reinforced nylon 6 composites,” *Polymer*, vol. 47, no. 13, pp. 4760–4767, Jun. 2006, doi: 10.1016/j.polymer.2006.04.020.

[50] M. Garg, S. Sharma, and R. Mehta, “Pristine and amino functionalized carbon nanotubes reinforced glass fiber epoxy composites,” *Compos. Part Appl. Sci. Manuf.*, vol. 76, pp. 92–101, Sep. 2015, doi: 10.1016/j.compositesa.2015.05.012.

[51] S. Ushiba, S. Shoji, K. Masui, J. Kono, and S. Kawata, “Direct Laser Writing of 3D Architectures of Aligned Carbon Nanotubes,” *Adv. Mater.*, vol. 26, no. 32, pp. 5653–5657, Aug. 2014, doi: 10.1002/adma.201400783.

[52] F. Cheng, Y. Hu, B. Yuan, X. Hu, and Z. Huang, “Transverse and longitudinal flexural properties of unidirectional carbon fiber composites interleaved with hierarchical Aramid pulp micro/nano-fibers,” *Compos. Part B Eng.*, vol. 188, p. 107897, May 2020, doi: 10.1016/j.compositesb.2020.107897.